This paper must be cited as:

Sirazul Haque, Miguel Alexandre, Clemens Baretzky, Daniele Rossi, Francesca De Rossi, António T. Vicente, Francesca Brunetti, Hugo Águas, Rute A. S. Ferreira, Elvira Fortunato, Matthias Auf der Maur, Uli Würfel, Rodrigo Martins, and Manuel J. Mendes, ACS Photonics 2022 9 (7), 2408-2421, DOI: 10.1021/acsphotonics.2c00446

Photonic-Structured Perovskite Solar Cells: Detailed Optoelectronic Analysis

Sirazul Haque[1,2,*], Miguel Alexandre[1], Clemens Baretzky[3,4], Daniele Rossi[5], Francesca De Rossi[5], António T. Vicente[1], Francesca Brunetti[5], Hugo Águas[1], Rute A. S. Ferreira[2], Elvira Fortunato[1], Matthias Auf der Maur[5], Uli Würfel[3,4], Rodrigo Martins[1], Manuel J. Mendes[1,*]

[1] *CENIMAT|i3N, Department of Materials Science, School of Science and Technology, NOVA University of Lisbon and CEMOP/UNINOVA, Campus de Caparica, 2829-516 Caparica, Portugal*

[2] *Department of Physics, CICECO - Aveiro Institute of Materials, University of Aveiro, Campus Universitário de Santiago, 3810-193 Aveiro, Portugal*

[3] *Fraunhofer Institute for Solar Energy Systems ISE, Heidenhofstr. 2, 79110 Freiburg, Germany*

[4] *Freiburg Material Research Center FMF, University of Freiburg, Stefan-Meier-Str. 21, 79104 Freiburg, Germany*

[5] *CHOSE, Department of Electronic Engineering, Università degli Studi di Roma Tor Vergata, Via del Politecnico 1, 00133 Rome, Italy*

**Corresponding authors: s.haque@campus.fct.unl.pt, mj.mendes@fct.unl.pt*

Abstract

Recent experimental advances in perovskite solar cell (PSC) technology marked a new era for low-cost, flexible and high efficiency photovoltaics (PV). In contrast, the study of the detailed physical mechanisms governing the optoelectronic properties of PSCs has not been keeping up with these breakthroughs which have been eclipsing theoretical efforts aimed at a more in-depth understanding of this emerging PV technology. Consequently, this has been hindering the design of the devices from reaching their maximum potential. The present article aims to bridge this gap by using a coupled optical and electrical modelling approach to optimize and rigorously assess the transport properties of selected photonic-structured PSC architectures, with particular attention given to ultrathin (300 nm) perovskite absorbers as they can pronouncedly profit from the light-trapping effects provided by the micro-structuring.

The central finding of this study is that photonic structured ultrathin PSCs benefit from a significantly enhanced light in coupling, and subsequent photocurrent generation in the absorber layer. This leads to more than 20% increase in short circuit current in comparison with planar devices. In addition, slight increases in open-circuit voltage and fill factor can be obtained due to the ultrathin perovskite absorbers, and thus power conversion efficiencies approaching 30% are possible. Moreover, it was also found that the electrical simulations of complex 3D device geometries can be accurately simplified to 1D, massively benefiting the computational efficiency of these studies.

Keywords: Photovoltaics, Photonics, Perovskite Solar Cells, Coupled Optical and Electrical Modelling.

1. Introduction

Perovskite solar cells (PSCs) have stormed the solar cell community in the past decade, and are now considered the most promising emergent photovoltaic (PV) technology [1]. Their non-vacuum solution-processing, which does not require highly specialized installations or expensive equipment, enabled many researchers around the globe to fabricate high performance PSC devices. It also brought forth a wave of worldwide effort aimed at improving and mitigating the shortcomings of PSCs technology in many different aspects such as: efficiency, stability, flexibility, reduction of harmful materials, etc. [1–5]. Despite the extraordinary growth of the PSCs' power conversion efficiency (PCE, now >25.5%) [2] over the years, from a theoretical standpoint, there are still many aspects of their intrinsic behavior that are inadequately understood, particularly concerning electrical effects (i.e. ionic transport, charge recombination and trapping, interplay at interfaces, inhomogeneous field generation, etc.). Therefore, an in depth fundamental analysis of the PSC properties is crucial to close the gap to the maximum achievable PCE (~30%) [6,7].

In addition, there is now a growing market demand for flexible solar cells [8–10], namely for consumer-oriented applications whose devices are required to be ultra-thin to allow improved intrinsic mechanical bendability [11–14]. This, in part, requires a lower absorber material thickness, which is beneficial in PSCs as an effective means to attenuate the amount of hazardous/toxic compounds (e.g. Pb) present [4]. For instance, reducing the conventional 500 nm perovskite layer thickness to 300 nm, as analyzed in this work, would lead to a considerable 40% reduction in Pb content. Furthermore, reduced thickness can have manufacturing cost benefits, not only due to the lower material usage (representing a small, yet significant, contribution to total module expenses)[15], but also improving flexibility which allows better compatibility with roll-to-roll processing [16] and lower installation costs.

To counterbalance the significant drop in light absorption and, consequently, in the device efficiency caused by the reduction of the thickness of the PSC layer, it is essential to develop ultra-thin absorber layers with state-of-the-art optoelectronic properties [11–13]. The design of optical enhancement strategies is another essential approach to manage these lower thicknesses without forfeiting performance [4,6,17]. Moreover, it has been shown that the same optical strategies also improve the stability of the PSC layer, which is an important limiting factor for the commercialization of PSCs [17–19]. Several advanced optical enhancement strategies have been proposed, such as anti-reflective coating [20], scattering media [21], texturing the charge transport layers [22] and/or absorber [23], nanophotonic front [24] and back electrodes [19], disordered micro-structuring [25], light harvesting using up-/down- converter coatings or nanoparticles [17], including plasmonic effects [26]. Despite the performance gains, these methods are generally contrasted by other unwanted mechanisms, such as parasitic absorption, complex integration with solar cells or unrealistic scale-up [4].

One way to gain insight into the complex behavior of PSC devices is through the development of realistic simulation models, considering both optical and electrical effects [27] to account for carrier recombination,

irregular field distribution and, thus, accurately predict device performance and allow modelling-aided design optimization, which can be of utmost importance for this emergent PV technology based on ultra-thin and flexible solar cells [8,9]. However, most theoretical studies of light trapping in PSCs focus only on the optical effects at play [17], therefore not guaranteeing PCE improvement due to the lack of understanding of the behavior of LT-enhanced PSCs from an electrical standpoint, thus hindering the achievable gains for these devices.

To overcome these shortfalls, the present work developed a complete optoelectronic modelling procedure, from which it was determined that photonic-enhanced PSCs can indeed capitalize on the optical gains - particularly for ultrathin PSCs (perovskite layer: 300 nm) - and translate them to the electrical domain, thus achieving close to 30% efficiency. The starting point is a conformal architecture designed for maximum optical density that can be achieved by depositing the PSC layers independently onto optimally patterned substrates. Such fabrication methodology represents a novel research direction as well, since the enhanced generated photocurrent achieved outperforms the most sophisticated optical strategies reported, without sacrificing scalability by making use of industrial-friendly geometries and fabrication methods. Besides, the study presented here reveals that the developed photonic-structuring of the PSCs does not lead to a significant increase in surface recombination, and also the performance is not affected by the inhomogeneous field generation caused by interference of the light waves scattered from the micro-structuring. The band-alignments of the photonic-structured PSCs reveal to be favorable for the carriers' transport towards the contacts. Hence, the electrons generated can be collected, even in the dense photon trapping regions.

Consequently, it is shown that photonic-structured PSCs with ultrathin perovskite (300 nm, higher flexibility) can outperform conventional planar PSCs with thicker perovskite (500 nm, rigid), and the electrical (PCE) performance improvement can be even slightly higher than the optical (photocurrent) enhancement caused by light-trapping (LT).

This work constitutes an important step towards high performance devices geared for consumers, such as portable electronics, BIPV, light-harvesting semi-transparent windows [28], wearable PV, solar-powered vehicles and self-powered smart electronics, which are promising PV market drivers. In addition, the design of the optical schemes presented herein shows great potential to be forthwith incorporated in high-efficiency tandem (double-junction) [29–34] and triple-junction [35,36] PSC devices.

2. Methodology and Experimental considerations

A complete optoelectronic study of different photonic-structured PSC configurations was performed by optimizing first its design from an optical standpoint, depicted in Figure 1a, and then by using the resulting

carrier generation profiles as input for the electrical drift-diffusion model of the devices, following the process flow shown in Figure 1b. The photonic features are modelled with a spheroidal geometry that is patterned on the substrate supporting the solar cells, in both superstrate-type and substrate-type PSC architectures, and arranged in a hexagonal array (honeycomb lattice). The five PSC layers are taken to be conformally deposited onto the substrate micro-patterns, as sketched in Figure 1a.

The Ansys Lumerical© FDTD [37] Solutions package was used to perform the complete optical analysis of the devices, due to the robustness and versatility of its finite-difference-time-domain (FDTD) algorithm, which can be used for electromagnetic simulations of arbitrarily shaped media. In addition, its ability to do single-run broadband simulations is also very beneficial for PV. The details regarding the FDTD simulation process and setup, including the refractive index spectra of the modelled materials, are provided in section S1 of Supplementary Material (SM).

To adequately optimize the structures to achieve the ideal device dimensioning, several parameters need to be evaluated concerning the geometry of the photonic features (in-plane, R, and normal-to-plane, R_Z, spheroidal radii), array periodicity (pitch, p) and the thickness of the layers (t_{layer}), being the optical photocurrent, J_{PH}, the initial Figure of Merit. For that, stochastic optimization approaches are preferred due to their more efficient search within vast parameter spaces [11]; hence in this work, a particle swarm optimization algorithm (implemented in the FDTD solver) was used to achieve the device dimensioning that maximizes J_{PH} (more details given in section S1 of SM) [4,11].

The FDTD optical results were then combined with a finite volume method (FVM) and a finite element method (FEM) implementation of the charge transport equations (drift-diffusion plus Poisson), to model the electrical behavior of the devices. Three different solvers (TiberCAD [38], Lumerical-CHARGE [39], and Sentaurus Tcad [40]) were used to compare and corroborate the results. Standard values of the electronic properties of the cell materials were obtained from the literature and used as inputs to the electrical simulations. The collected literature values include, among others, the bandgap, dielectric permittivity, electron/hole effective mass, electron affinity, mobility, lifetime, doping, the density of states and series resistance (more details in section S2 of SM) [41,42]. Due to the complexity of the electrical simulations, in particular for PV technologies such as PSCs involving a combination of organic and inorganic compounds, the modelling results obtained were also compared with experimental results for conventional planar PSCs, to both provide a strong reliable foundation for the simulation setup as well as to further refine the parameters of the device. A detailed description of the simulation process is provided in section S2 of SM.

While planar multilayered solar cells can be accurately modelled via 1-2D simulations, the same may not be ensured for photonic-structured devices like the ones under study (Figure 1a), which demand higher modelling dimensionality (2-3D). However, since the exact electrical modelling becomes significantly more complex with an increase in dimensionality, simulations were also performed at different

dimensionalities to compare 3D simulations (the most accurate geometric representation, but most limited in spatial resolution) with their 2D and 1D counterparts for a better insight into the real impacts of such simplifications.

From the complementarity of the optical and electrical results, it is possible to understand the main underlying physical mechanisms governing the response of the PSCs, with and without photonic structuring, thus enabling a complete modelling-aided design of the devices.

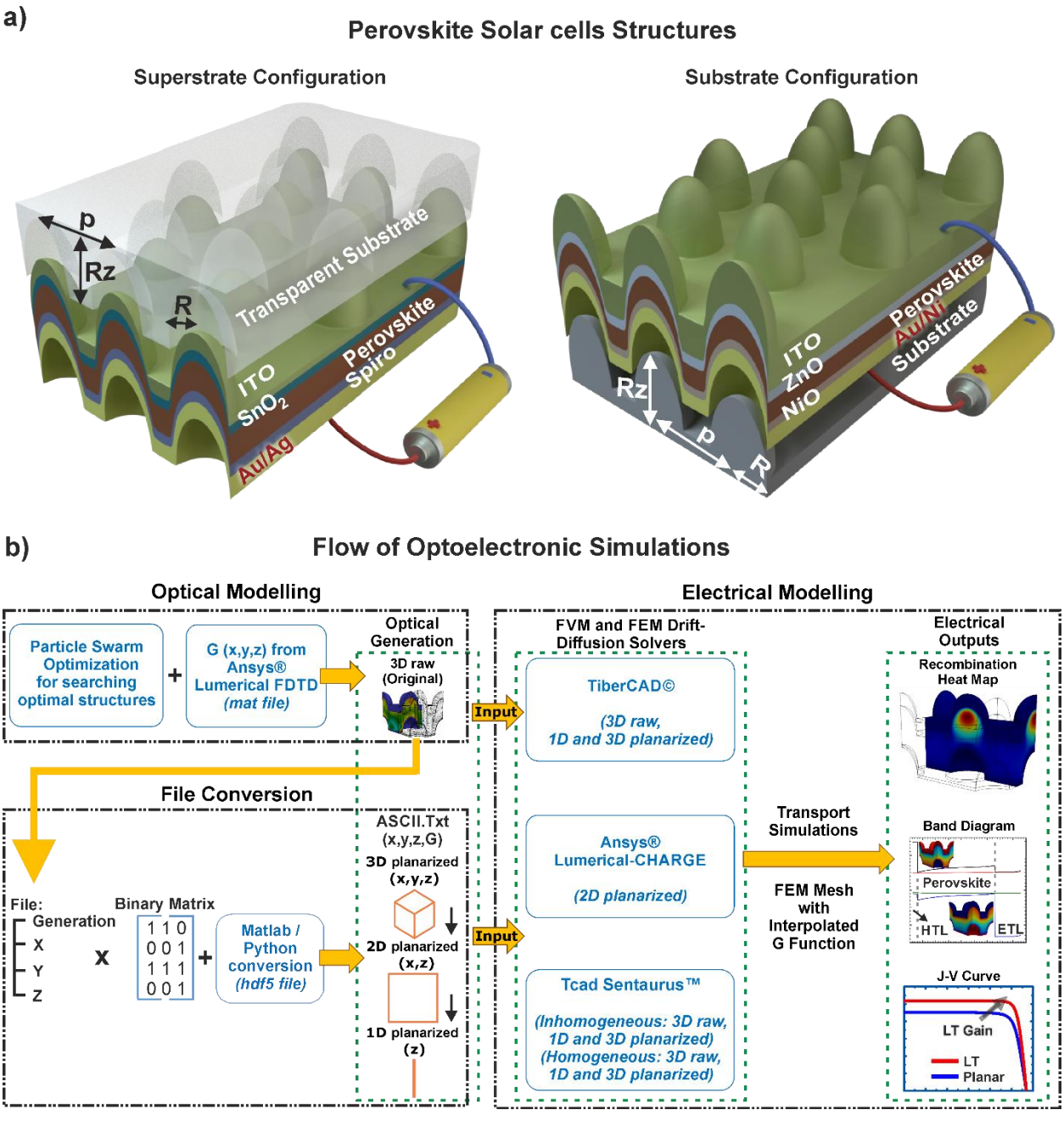

Figure 1: The photonic-structured substrates were studied and optimized for two types of PSC architectures with different metal contacts (Au, Ag and Ni): the conventional superstrate configuration (Fig. 1a, left) in which light enters from the transparent substrate, and the so-called substrate configuration (Fig. 1a, right) in which light impinges on the cell side. The LT structures patterned on the substrates are modelled as a hexagonal array (with pitch *p*) of vertically-aligned semi-prolate features with radii *R* and R_Z, respectively along the in-plane direction and illumination axis. The PSC layers are then conformally deposited over such spheroidal structures. Coupled optical and electrical simulations were performed to assess the full optoelectronic response of the solar cells following the process flow shown in b). First, 3D optical (electromagnetic) simulations are carried out using the FDTD solver, incorporating a particle swarm algorithm that optimizes the geometry of the photonic-structured PSCs. This was followed by the electrical simulations, here employing three FVM/FEM solvers for comparison and validation, which take as input the 3D-optically obtained generation profiles (original, raw *G*) from the FDTD solver as well as 3D, 2D or 1D planarized generation profiles resulting from planarizing the original *G* function using a binary matrix (3D-planarized) and further decreasing it to lower dimensions (2D and 1D planarized) when needed. Moreover, the electrical simulations were also carried out considering conceptual homogeneous (i.e. spatially-independent) generation profiles with a fixed value across the absorber region equal to the volume-averaged *G*.

3. Results and Discussion

3.1 Optical Modelling and Wave Optical Physics

The semi-spheroidal LT structures provide a combination of geometrical gradual index matching and light scattering properties to, respectively, suppress reflection and effectively trap light inside the solar cells. These structures have also been shown to provide a broad angular acceptance, which is paramount for the proper functioning of the devices under bending conditions [4]. In terms of manufacturability, the studied geometry of semi-spheroidal features in a hexagonal (honeycomb) array mimics the photonic designs that can be fabricated by industrially-attractive micro-patterning methods such as colloidal lithography (CL) - a low cost soft-lithography process capable of engineering the optical schemes with nano/micrometer resolution with high uniformity and in a highly scalable manner [43–47].

The PSC layers are then wet-coated onto the patterned substrates, thereby becoming photonic-structured due to conformal deposition, as sketched in Figure 1a. Such approach requires adapted deposition methods to allow conformability of the PSC layers onto the corrugated substrates [32,33,46], but this strategy has practical benefits compared to other LT implementations [11] based in post-patterned photonic structures (e.g. coatings) implemented over the PSCs with flat perovskite layers, because the micro-structuring process may involve fabrication steps (e.g. immersion in water and exposure to plasma etching in CL)[44,47,48] that can be harmful to the PSCs. Therefore, to prevent the LT implementation from deteriorating not only the PSC layers but also less robust polymeric substrates used in flexible devices [12,49], it is advantageous to deposit the PSC

layers by usual methods over a substrate already patterned with LT structures, as proposed here. In this way, the photonic integration becomes independent of the PSC's fabrication.

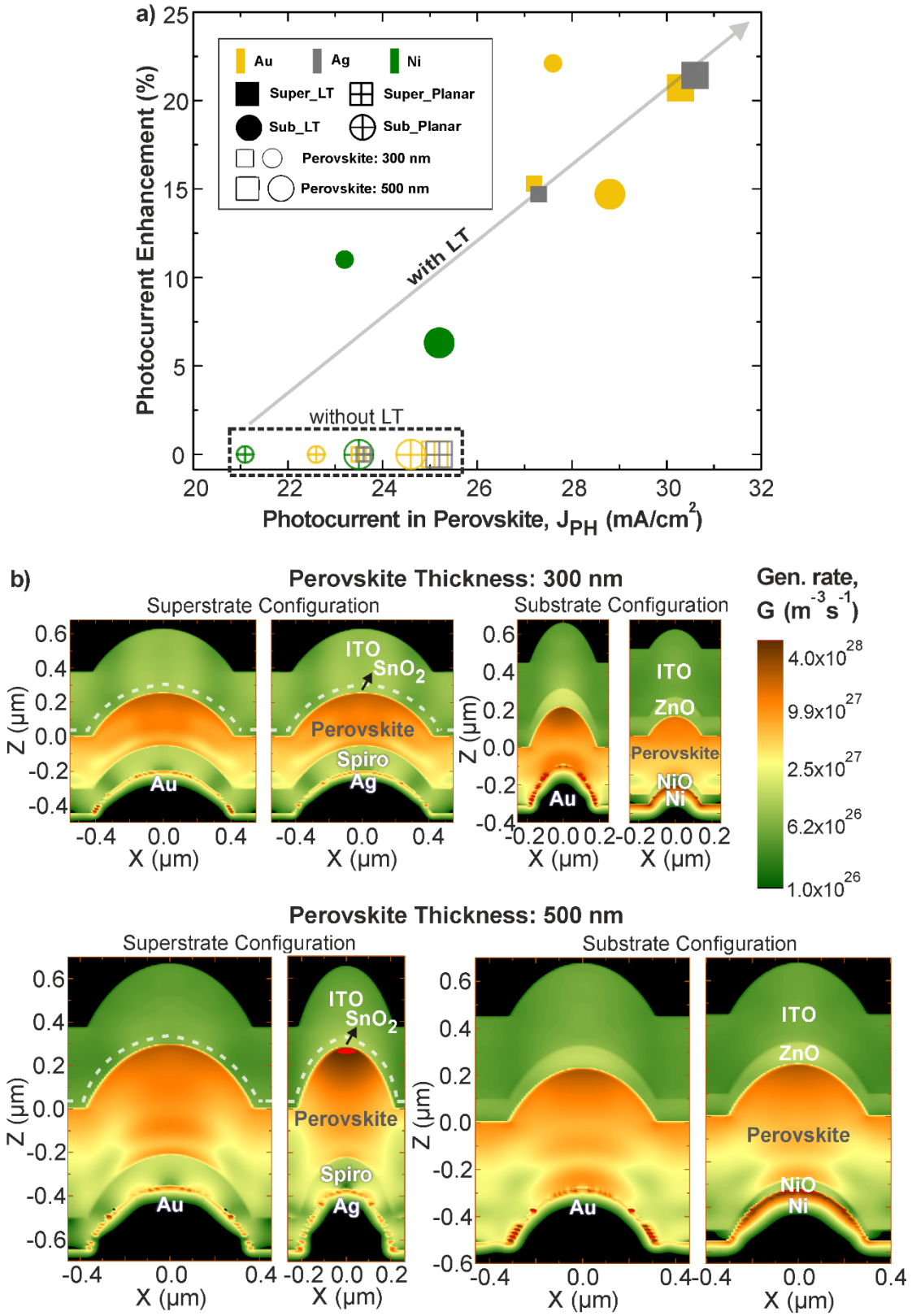

Figure 2: Improvement in photocurrent density (a), J_{PH}, achieved with the optimized photonic-structured PSCs for different cells configurations, metal contacts and distinct perovskite thicknesses (as shown in Table S1 of SM), relative to the planar references as indicated on the horizontal line (a). The profiles represent the total generation rate, *G*, along the xz cross-sectional plane of the structures for all the photonic-structured PSCs studied here (b).

Apart from analyzing different PSC configurations, the influence of alternative materials on the PCE was also assessed. Namely, the properties of the rear metal contact were found to be particularly crucial for LT performance. Au is the metal contact of choice for PSCs, but its high cost brings a strong negative impact on the devices' scalability. Therefore, Ag and Ni were studied here as more affordable alternatives. Different materials for the electron transport layer (ETL) and hole transport layer (HTL) were also considered: SnO_2 and ZnO were chosen for the ETLs, as they have shown better stability over typical TiO_2 [50], and Spiro-OMeTAD and NiO_x for the HTL, since the inorganic NiO_x has also revealed stability benefits relative to the conventionally-used organic Spiro-OMeTAD [51]. In addition, the cell layers' thicknesses are considered within reasonable ranges in accordance with the state-of-the-art of PSC technology (e.g. the minimum thickness allowed for the TCO, made of ITO, is 350 nm in the PSO optimization algorithm) [52].

We begin by optimizing the LT structured substrates (illustrated in Figure 1a) to achieve maximum photocurrent (J_{PH}) using the particle swarm optimization algorithm. Figure 2 summarizes the optimization results for the different structures (Figure 2a), and shows the cross-sectional optical generation rate (G, see Figure 2b) for comparison between different structures – 300/500 nm thick perovskite in superstrate and substrate configuration. From Figure 2a and Figure S2 of SM, one can see that, in all cases, the photonic-structured PSCs with ultrathin (300 nm) perovskite layer outperform the planar PSCs with the conventional (500 nm) perovskite thickness. For comparison, in section S1.1 of SM it is also presented the optimized results for an even thinner (150 nm) perovskite absorber, which gives a higher photocurrent gain (22.8%) relative to the planar counterpart, as expected from theoretical Lambertian analysis [11], but an absolute photocurrent (23.7 mA/cm^2) already below that (25.1 mA/cm^2) of the 500 nm planar PSC.

The Ag contact allows similar performance as Au, while Ni contacts are optically worse in general. Nevertheless, the photonic-structured PSCs with Ni can perform as well as the optimized planar PSCs with Au and Ag metal contacts, as seen in Table S1 of SM. Therefore, Ni is still a good candidate for PSC application, also if we consider its low price and the industrial advantage of allowing the fabrication of the NiO_x HTL layer simply by oxidizing the Ni rear contact in the same process run [53].

The observed gains (also presented in the absorption profiles in Figure S2 of SM) are chiefly governed by two different optical mechanisms: anti-reflection (i.e. light in-coupling) [11,16,54] and light scattering properties [11,16]. The enhanced anti-reflection effect is predominately achieved from the geometrical index matching of the real part (*n*) between the semi-spheroidal structured front layers (TCO, ETLs and perovskite). This effect is mostly responsible for enhancing absorption in the UV-VIS range, due to the superior light in-

coupling towards the absorber (perovskite) material. At the same time, strong near-field forward-scattering occurs because of the micro-lens effect arising from the optimized curvatures of the front layers, which generates high intensity electric fields in the top portion of the perovskite layer, as observed in the G profiles of Figure 2b. In this range below ~700 nm wavelength, light is easily absorbed by the cell, so that reflection in the back contact has a much-decreased impact on the overall absorption. For longer wavelengths (NIR region), the absorption enhancement is mostly governed by the far-field scattering caused by the semi-spheroidal shape of both the front and rear features of the photonic-structured PSCs, which benefits as well from the high real part (n) of the perovskite refractive index. This effect manipulates the light that falls vertically and redirects it to paths closer to the horizontal plane, thus leading to optical path increase and easier coupling into waveguided modes trapped in the absorber layer. This is evidenced by the "hot spots" observed in the rear side of the perovskite material, shown by the optical generation (G) profiles of Figure 2b. These "hot spots" result from the constructive interference between the light waves traveling along the incidence direction and the scattered light traveling along the plane of the cell layers that suffer multiple reflections from the top and bottom surfaces of the cell. As such, the sharp absorption peaks seen in the NIR in Figure S2 of SM are a consequence of the 3D Fabry-Perot resonances resulting from such interference.

The response of the solar cells with the variation of the geometrical parameters of the structures (R_z, R, p) around the optimal values was also analysed, focusing on the photonic-enhanced PSCs with 300 nm thick perovskite layer (see Figure 3). It further clarifies the above optical phenomena, since the influence of the structures' height, R_z, in the absorption enhancement for shorter wavelengths in UV-VIS is higher than for longer wavelengths in NIR, since R_z mostly affects the anti-reflection gain due to the geometrical index matching. Conversely, the lateral radius, R, and array pitch, p, have minor influence on the absorption gains in the shorter wavelengths but have a strong effect for the longer wavelengths. R and p set the grating properties of the LT structures, which determine the guided-mode trapping in the longer NIR wavelengths. In general, it is noticeable that the photocurrent remains not far from the maximum within large (± 10%) variations of the geometrical parameters, demonstrating that the designed semi-spheroidal LT structures are adequately tolerant to fabrication imperfections, which is a key advantage from an industrial perspective.

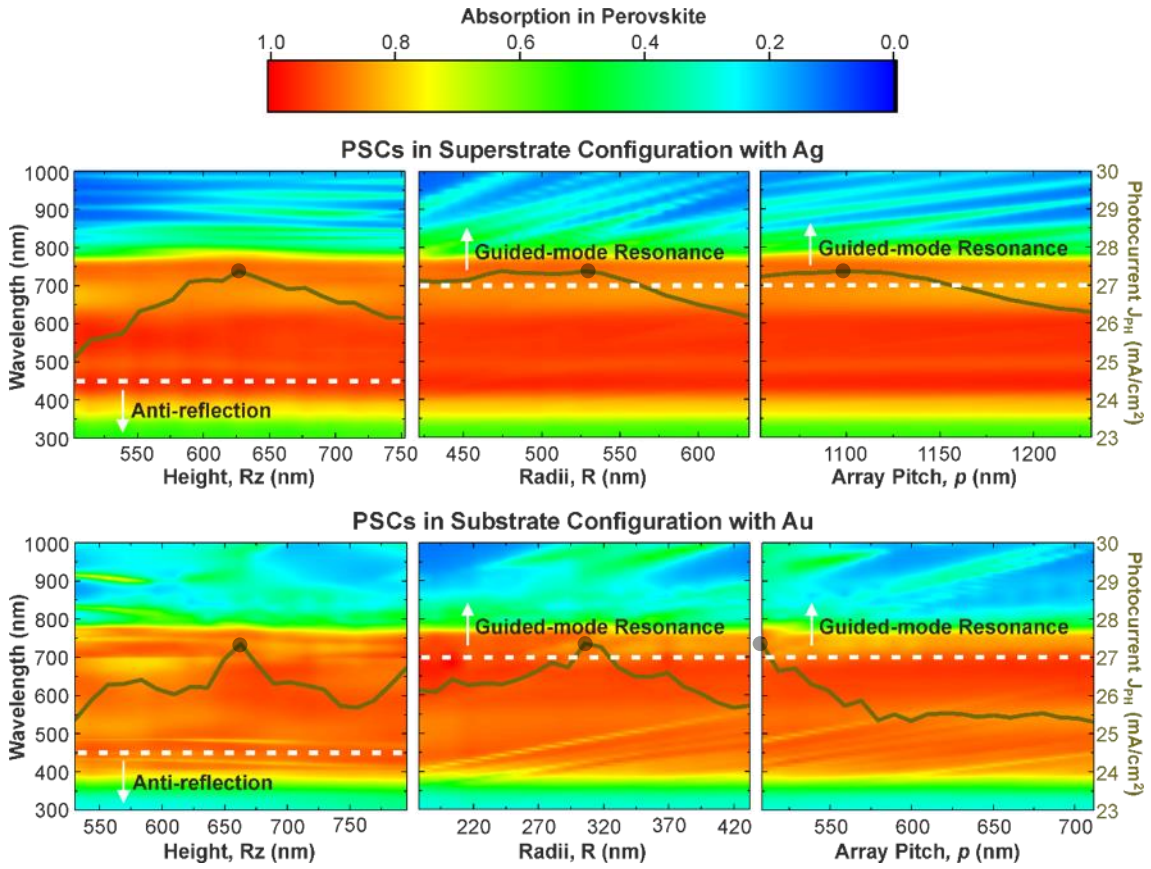

Figure 3: Spectra of the absorption in the perovskite and photocurrent density (J_{PH}, dark line) attained with a 20% variation (±10% deviation) in each geometrical parameter (R_Z, R and p), relative to the optimal parameter values marked by the circles in the dark line (indicated in Table S1 of SM). This is shown for two cases of the photonic-enhanced PSCs with 300 nm thick perovskite layer and metal contact of Ag (*top plots*) or Au (*bottom plots*), in superstrate and substrate configurations, respectively. The white dotted lines qualitatively separate the effects of anti-reflection (stronger influence below ~450 nm wavelength) and guided-mode resonances (stronger influence above ~700 nm wavelength).

3.2 Electrical Modelling and Device Physics

There has been an increasing interest in the PV-related community for the development of coupled optical and electrical models capable of exactly predicting and optimizing the full response of optoelectronic devices [55], as developed in this work and applied to the challenging case of photonic-structured PSCs.

As previously described (Figure 1b), this process involves a two-step approach: 1) detailed simulation of the solar cell optical response with an electromagnetic FDTD formalism, as presented in the previous section 3.1; and 2) the optical results are then used as input for the FVM and FEM model that determines the electrical behavior of the device, as the current density vs. voltage, *JV*, characteristic curve. Such approach has been thoroughly reported and extensively studied for the modelling of common (inorganic)

PV semiconductor materials and cell architectures (single-junction and tandems) [42], whose behavior can be directly described by the traditional drift-diffusion formalism. However, the charge transport properties of solar cells composed of novel materials, as the hybrid organic-inorganic perovskites addressed in this work, have yet to be more clearly understood, in close interaction with experimental characterization. Namely, two main aspects make the electrical modelling of PSCs particularly complex:

1) heterojunction configuration - specifically the formalism employed by the numerical FVM and FEM solvers of the drift-diffusion/Poisson equations can break down with sharply varying electric fields, which is an intrinsic characteristic of heterojunctions as those in PSCs (namely at ETL/Perovskite/HTL interfaces [56]);

2) non-standard mechanisms observed, e.g. attributed to the presence of mobile ionic charge species in the perovskite, which can pronouncedly affect the optoelectronic response of PSCs, such as the JV hysteresis (i.e. the JV dependence on the direction/speed of the bias scan [57]), that cast doubts and make their charge transport behavior nebulous when compared to standard inorganic materials as c-Si.

In addition, the micro-structured PSCs studied here provide additional challenges, chiefly due to the curvature of the structures that increase the surface area and generate “hot-spots” (densely illuminated regions inside the cell). The “hotspots” derive from the locations of constructive interference of the light waves established within the periodically-structured devices, which can make their charge generation and transport properties more complicated when compared to planar cells.

Even though the actual charge-transport mechanisms in hybrid-perovskites can be influenced by their organic parts, it has been observed (mostly in high-performing devices) that it can be accurately modelled by approximating it to an inorganic semiconductor, even presenting properties resembling those of GaAs [58]. The same logic applies to the contact layers (HTL/ETL), where their hole/electron-separation role is modelled through fitting parameters that are as close as possible to the values known for these materials [56].

Here, a thorough assessment was first performed on the material parameters used for the electrical simulations, based on fabricated high-efficiency flexible PSCs as described in sub-section 3.2.1. Subsequently, the different optically-optimized photonic-structured devices, in both superstrate and substrate configurations, were electrically modelled as described in section 3.2.2. Lastly, we explored the ultimate efficiency that can be achieved using LT, by considering the state-of-the-art highest efficient PSCs, as well as investigating the dimensionality of the simulation in the computed response, as described in section 3.2.3.

3.2.1 Electrical modelling and validation with experimental results

Given the promising application of photonic-enhanced PSCs for bendable devices [11], a potentially-flexible planar PSC deposited on PET substrate with high efficiency (measured PCE=18.5%, see Figure S5 in SM) was taken as a reference to extract the relevant electrical parameters (effective mass, bandgap, recombination properties, etc.) of the materials and refine the simulation model. The parameters used are summarized in section S2.1 of SM. For the fitting procedure, a simple 3D-optical/1D-electrical model implemented in TiberCAD was used. This benefits from significant improvements in simulation time and memory requirements, without the loss of accuracy in the results, since for flat multi-layered structures the optical generation only changes in the direction of light propagation (*z* axis). As such, for the electrical simulation, the 1D optical generation was obtained by averaging $G(x,y,z)$ in both the *x* and *y* directions.

While 1D electrical simulations are sufficient for the accurate modelling of conventional planar PSCs, as in Figure S5 in SM, when considering structured devices such simplification in dimensionality needs to be reassessed as the optical generation profile is no longer uniform in x/y. The complex 3D behavior of the generation profile in the cases of the photonic-structured PSCs of Figure 1 can have a non-trivial impact when averaging the generation profile in the in-plane dimensions, which may lead to errors in the calculation. Hence, the rigorous 3D-optical/3D-electrical model to simulate the photonic-structured devices developed for this work and based on the electrical properties extracted from the experimental comparison (Figure S5 in SM).

Substrate-type PSCs, as shown in Figure 1a, were first modelled for a planar and photonic-structured device, using the previously mentioned set of material parameters. The planar cell [structure: Au (200 nm)/NiO_x (10 nm)/Perovskite (300 nm)/ZnO (100 nm)/Au (100 nm)] was simulated for both 1D-electrical and 3D-electrical cases. The current obtained was 22.6 mA/cm^2 for both simulations, thus reinforcing the validity of the above-made approximation. The photonic structured devices have the optimized hexagonally symmetrical structure (see Table S1 in SM) with period p=508.4 nm and radii R=254.2 nm and R_z=662.8 nm. The 3D charge carrier generation profiles obtained are shown in Figure 4a, b for the planar and photonic-structured PSCs. The optical modelling of these structures in section 3.1 pointed to a current density of J_{PH}=27.6 mA/cm^2, while the electric modelling resulted in a lower value of short-circuit current density J_{SC}=26.0 mA/cm^2. A lower value of J_{SC} is expected in the electrical simulations due to transport losses (mainly bulk and surface recombination) that are present in the drift-diffusion model, as well as because of the sampling error given by the different mesh sizes in optical and electrical modelling. Figure S6 of SM shows the radiative and Shockley-Read-Hall (SRH) recombination profiles for planar and LT-enhanced PSCs, where it is noticeable that SRH is the dominant recombination mechanism in the devices.

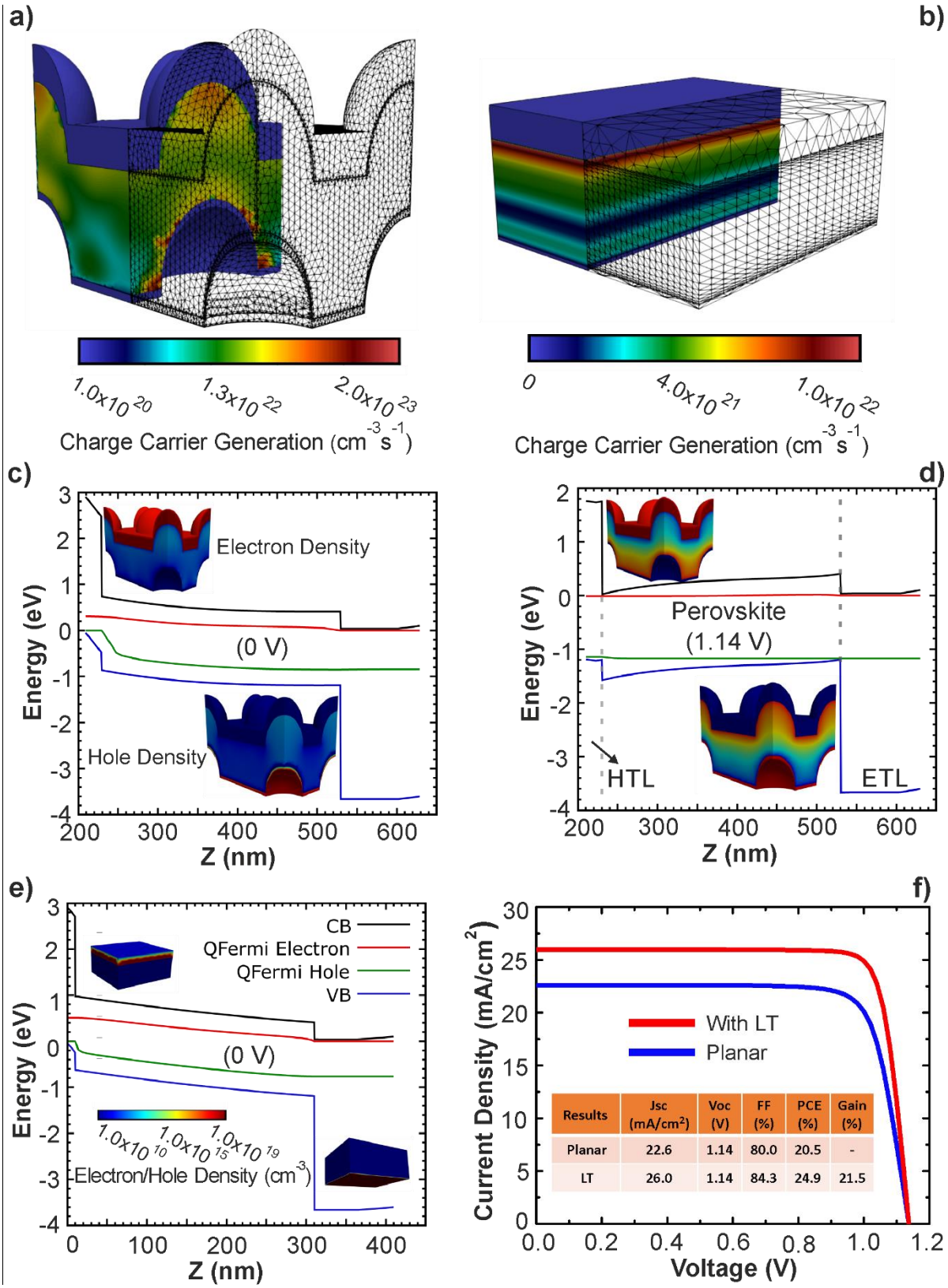

Figure 4: Comparison of electrical simulations of LT-structured and planar PSC. The 3D current generation profiles of LT (a) and planar (b) cells are shown together with the FVM and FEM simulation mesh. The plots in c,d) and e) represent the corresponding band diagrams for the LT (polarized at 0 and 1.14 V, respectively in c) and d) and planar

(at 0 V in e) cells. The 4 curves in the band diagram (c,d,e) represent the conduction band (CB) minimum, quasi-fermi electron (QFermi Electron) and hole (QFermi Hole) levels, and valence band (VB) maximum. The inset images in (c,d,e) show the free electron and hole density used in the electrical simulations. The resulting J-V curves of both planar and LT-structured PSCs are presented in f).

Figures 4c,d,e demonstrate that both LT and planar substrate cells have the same energetic band alignment, which is the expected behaviour. The band diagram should only depend on the materials used and not on the micro-structuring. It is observable from Figure 4d that at voltages close to V_{OC} (1.14 V) an inverse slope for the transport carriers appears in the perovskite bands. Such slope is not present at 0 V (Figures 4c,e) and can be correlated to the trapping and recombination of carriers before collection by the transport layers. The closer the polarization is to V_{OC}, the higher the recombination, up to the point where an equilibrium between generation and recombination of carriers occurs and the V_{OC} condition is achieved [59].

Nevertheless, from Figure 4f one can see that the higher degree of light confinement (absorption) attained with the photonic-structured PSCs significantly improves the photocurrent and, consequently, the efficiency. The studied planar cell with 20.5% efficiency can increase to 24.9% with the optimized photonic-structured counterpart, which represents a 21.5% gain. This enhancement is close to the 22.1% optical photocurrent gain computed in section 3.1 for the same photonic-structured PSC (Figure. 2a and Table S1).

3.2.2 Electrical modelling of photonic-structured PSC architectures

As described in the previous section, photonic-structured solar cells can be exactly modeled by 3D simulations, but the tradeoff is the highly demanding computational time and memory requirements. Yet, it is known that the high mobility of the perovskite material allows the carriers to travel quickly to the contact layers. Therefore, the authors propose the hypothesis whereby accurate electrical simulations can equally be obtained by planarizing and decreasing the 3D-optically obtained results to lower dimensions, which would reduce the computation time significantly. As such, the 3D-optical generation profiles, for both superstrate and substrate photonic configurations with perovskite thicknesses of 300 and 500 nm (i.e. for all the enumerated cases in section 3.1), were planarized and then averaged in the *y* in-plane dimension, resulting in a 2D generation profile to be used in the electrical simulations performed using Lumerical-CHARGE.

For the perovskite material ($CH_3NH_3PbI_3$) the charge transport is considered to be equal for both electrons and holes, although asymmetric transport is possible (e.g. by chloride addition into the iodide mixture; $CH_3NH_3PbI_{3-x}Cl_x$ [60]). Recently, the asymmetric featured HTL, synthesized by benzotrithiophenes small molecules, unveils full planarity that improves intermolecular π-stacking and charge transport, thereby leading to efficient HTL and higher efficiency PSCs. [61]. Furthermore, the complex behavior of the CH_3NH_3

ions can, in some cases, create hysteresis in the JV curves, as reported by several authors [57]. However, this behavior becomes much less pronounced in the highest-efficiency PSCs [62], so it is disregarded here. The ETLs (SnO_2 or ZnO) and HTLs (Spiro-OMeTAD or NiO_x) were modeled as semiconductors with doping profiles defined using a selective junction model, whose profile essentially depends on the density-of-states (DOS) of the materials set for the layers [41]. The electrode layers (ITO, Au) were taken as standard metallic materials described solely by their work function, Φ. The set of parameters used for the electrical simulations is provided in section S2.2 of SM.

Figure 5 depicts the resulting JV curves attained by the 2D simulations for the planar references and their photonic structured counterparts. The main quantities resulting from these curves are summarized in the inset tables and are in good agreement with the most recent experimental values of high efficient PSCs [1,2]. We also note that the response of the planar PSC with 300 nm perovskite is in good agreement with the previously calculated 1D simulation in section S2.1 (Figure S5) of SM, again reemphasizing the benefits of computationally efficient 1D simulation to model planar PSCs. The presence of photonic structures leads to a pronounced enhancement of the broadband light absorption across the perovskite layer, boosting the J_{SC}, while keeping the V_{OC} almost unchanged and only slightly reducing the FF following the 3D simulations presented in Figure 4. This results in overall PCE gains up to 25.4% due to LT, close to the optical photocurrent (J_{PH}) enhancements plotted in Figure 2a and listed in Table S1 of SM.

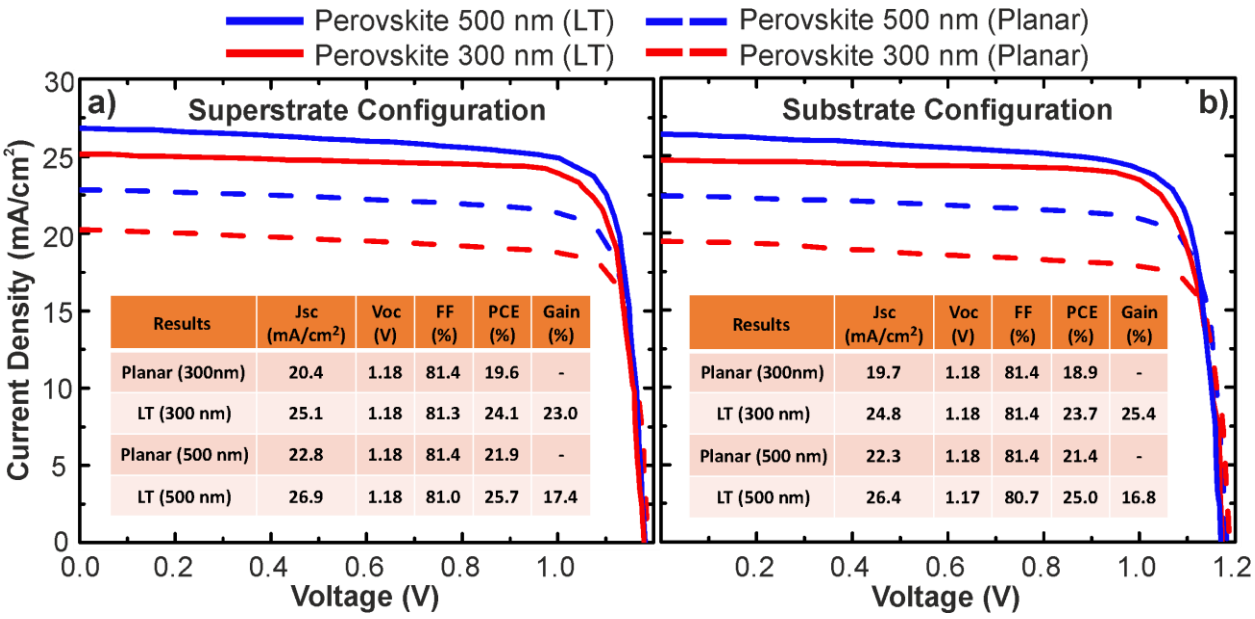

Figure 5: Simulated J-V curves of the PSCs with the conventional 500 nm and thinner 300 nm perovskite layers for both superstrate (a) and substrate (b) configurations. The inset tables present the PV quantities of interest for the simulated devices.

It is also observed that the J_{PH} values described in section 3.1 are consistently higher than the electrical J_{SC} values attained here. This is expected, since in the optical J_{PH} calculation all photo-generated carriers contribute to the current generated by the cell, while the J_{SC} takes into account the relevant electric losses within the layers and interfaces of the PSC structure, as a consequence of insufficient carrier transport (due to built-in E-field, recombination, potential barriers, etc.). These aspects are further discussed in the following section 3.2.3, again employing rigorous 3D simulations since the averaging (along y-axis) used for the 2D modelling prevents a complete assessment of the effects of surface recombination and inhomogeneous field distribution caused by the micro-structuring.

3.2.3 Analysis of interplay of interfaces and inhomogeneous generation in photonic-structured PSCs

Light management and interlayer engineering are two crucial factors to improve PSC efficiency. Here we combine the best optimized photonic structure with the approximated electronic properties of real, record-performing PSCs, in order to project the full potential of our LT scheme. We also address the question if, under these conditions, one can obtain accurate electrical simulations of complex 3D optical behavior by planarizing and projecting the 3D optical solutions to lower dimensions.

The selected architecture is the superstrate LT-structured PSC, with 300 nm perovskite thickness and Au rear contact (see Table S1 of SM for a summary of the dimension of the used features), whose main electrical parameters are listed in Table S4. Based on the selected structure and the assumption of physical parameters of the PSC close to the published world record [63–68], the set of electrical simulations presented in this sub-section explores the effects of three distinct physical parameters of the model:

1) **Dimensionality:** 3D vs. 1D electrical simulation, using the original 3D optical generation profile, $G(x,y,z)$, provided by Lumerical FDTD and shown in Figure 6a;
2) **Generation spatial distribution:** Inhomogeneous vs. homogeneous generation profile, in which a conceptual homogenous (constant) generation, $G(x,y,z)=\langle G \rangle$, is created by averaging the 3D-optical inhomogeneous generation across the absorber volume (see Figure 6b);
3) **Carrier recombination:** comparing the results with and without the effect of SRH recombination, shown in Figure S8 (b) in the perovskite bulk and interfaces. When neglecting SRH recombination we consider only radiative recombination, shown in Figure 6c, thus modelling a Shockley-Queisser-like scenario.

Firstly, we analyzed the maximum photocurrent (J_{PH}=27.2 mA/cm^2, see Figure 2) attainable from the 3D optical generation data, $G(x,y,z)$. Multiplying with the inferred volume of voxel (3-dimensional "grid point", i.e. grid unit cell) and summing to total generation rate yielded a short-circuit current density J_{SC}=26.96 mA/cm^2, which is just slightly below J_{PH} due to sampling errors, over the first complete

generation region without aliasing artifacts, which yields a 296.15 nm thick absorber, and multiplying the average with the full absorber thickness results in J_{SC}=27.08 mA/cm^2. Further clarification on the data process from Lumerical into Sentaurus Tcad is given in section S2.3 of SM. The adjusted J_{SC} corresponds to an average generation rate of $\langle G \rangle = 5.628 \times 10^{21}$ cm^{-3}s^{-1} integrated for the absorber volume. This is the reference value used in the subsequent simulations that considered a homogeneous (constant) generation profile equal to $\langle G \rangle$ for the entire perovskite material, as shown in Figure 6b. The comparison of the *J-V* curves for inhomogeneous and homogeneous generation emphasizes the electrical effect of the spatial distribution of the photo-generation, and the increased interface area caused by the photonic structuring. For a direct comparison, the integral over the original generation profile within the absorber needs to be equal to the integral over the homogenous generation profile. Therefore, the homogenous generation rate was set up to generate as many charge carriers as the inhomogeneous generation rate.

For comparing the results between the 3D and 1D electrical simulations for the structured PSCs, the 3D-optically computed $G(x,y,z)$ data needed to be adequately normalized for the 1D simulations (as sketched in Figure 1,b) by first planarizing the 3D generation profile, G, and then integrating along the in-plane directions (x,y), thereby creating the 1D generation profile, shown in Figure S8 (a) of SM. For the 1D electrical simulations of homogenous generation, a constant generation profile (similar to the 3D, as shown in Figure 6, b) equal to $\langle G \rangle$ along the *z* axis was used as shown in Figure S8 (a) of SM. Here, to properly compare the influence of the increased surface area (and also dimensionalities) due to the curved structures (photonic-structured devices) to the planar structure (planarized devices), all electrical parameters as shown in Table S4 (including surface and bulk recombination coefficients) were kept the same in both cases. Finally, to analyze the effect of carrier recombination, the 1D and 3D simulations were performed with and without the SRH coefficient, which is the dominant recombination mechanism.

For the considered set of parameters listed in Table S4 of SM, Figure 6 highlights how the outcome of the drift-diffusion simulations does not seem to be strongly correlated with the structural geometry of the solar cells. The changes in PV performance are almost negligible, as seen in Table 1, which is mainly a consequence of the high mobility of the carriers in the perovskite material, aided by the ultra-low thickness of the perovskite layer (300 nm). The combination of both factors allows the charge carriers to quickly travel from the dense photon-trapped regions (localized “hot-spots”) towards the contact layers where they can be extracted. Nevertheless, one needs to define the parameter space more concisely, i.e., which materials and interface parameters increase the sensitivity of the simulations to the device geometry, to a point where the geometry must be explicitly considered to obtain reliable results.

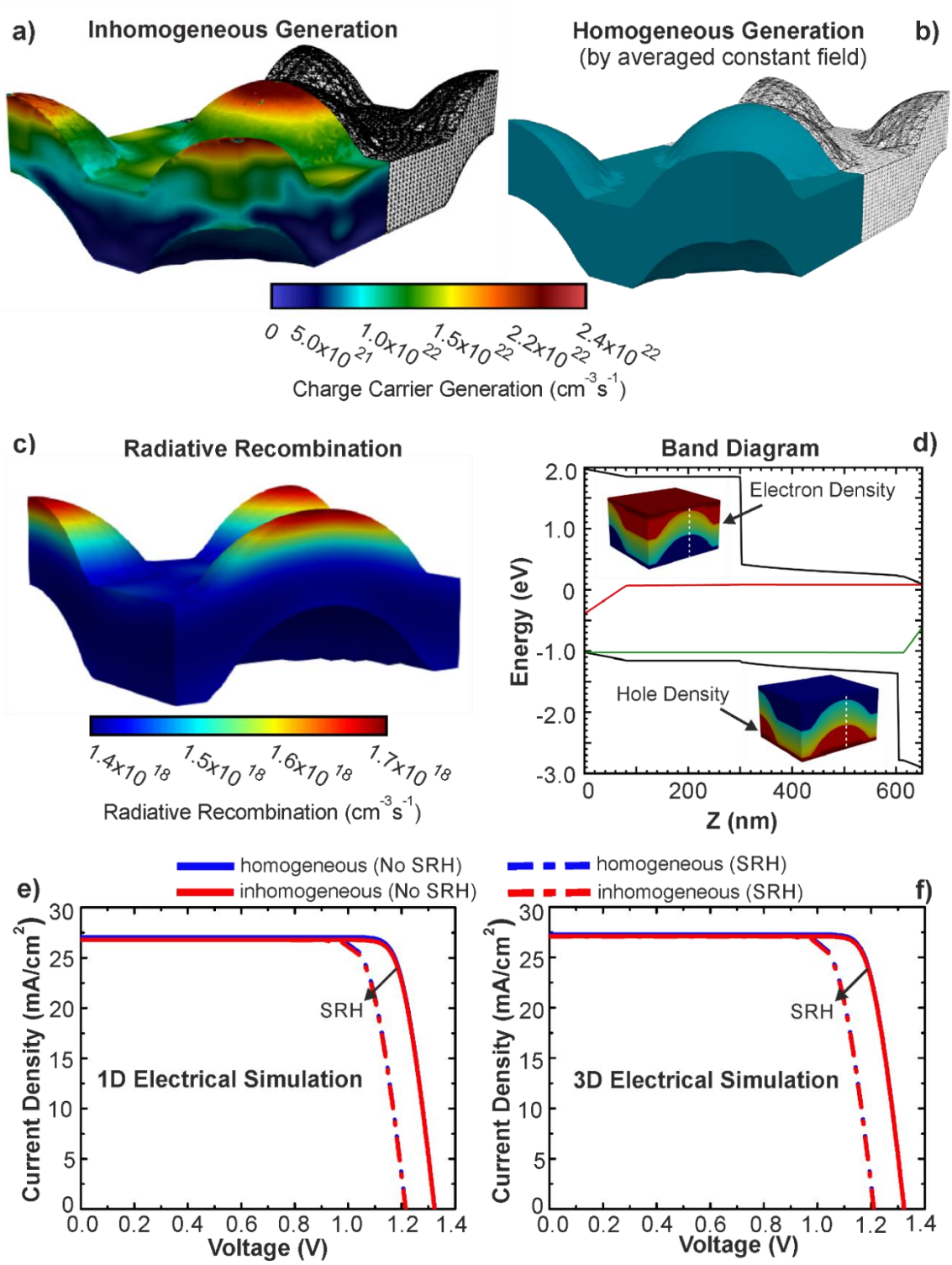

Figure 6: a, b) 3D inhomogeneous (original) and 3D homogenous (averaged) generation profiles used to evaluate the electrical PV performance. c, d) represent the radiative recombination profile at the maximum power point (c) within the perovskite absorber, and the band diagram of the structured PSC (d). e) J-V curves of the 1D (e) and 3D (f) device modelling using either the inhomogeneous or homogenous generation profiles, as well as with and without the effect of SRH recombination.

However, it can be said that electrical 1D simulations based on averaged optical generation can be regarded as a very good approximation of 3D approaches, as the PV outcomes are found to be almost identical to the inhomogeneous generation profiles. More generally, it can be inferred that the better the overall device performance with regard to carrier extraction and interface recombination the better the agreement between 1D and 3D simulations.

The moving from 3D to 1D computation is extremely important, as this change can speed up simulations by several orders of magnitude while reducing memory footprint. As an example, a typical 3D simulation of a photonic-structured PSC requiring about 16 hours and 128 Gb of memory, is reduced to 1.5 min and 30 Mb of memory when performed in 1D. Furthermore, it consolidates novel simulation techniques that can be used to study a broader range of devices.

Concerning the recombination effects, Figure S8 (b) of SM and Figure 6c depict the distribution of the two types of recombination mechanisms considered here: SRH (at interfaces and in the perovskite bulk) and radiative recombination. The SRH bulk and surface recombination parameters were chosen to reduce V_{OC} by 100 mV, respectively, or 140 mV when combined. While nonradiative recombination is generally considered to be the dominant loss mechanism in the highest efficiency PSCs, the distribution between bulk and interface is difficult to assess [7]. As such, a 50% contribution between the interfaces and bulk has been assumed. As expected, with activated SRH-recombination V_{OC} is significantly reduced. We note that the simulated interface area increases by 16% for the investigated photonic-structured PSC compared to the planar geometry, which leads to an increase in surface recombination. This in turn leads to an additional 5 mV reduction in V_{OC} for the photonic-structured PSC compared to the 1D structure, irrespective of the generation rate profile. Due to idealized extraction and a negligible influence of a potential shunt/parallel resistance, there is no slope observed at 0 V (J_{SC}) as seen in Figure 6d.

Overall, the electrical simulations using the optical generation profiles, originating from the advanced light-trapping structures computed by 3D FDTD, demonstrate the large potential gain for efficiency improvement of PSCs. Even though the study was not thorough in respect to the materials parameters, it does suggest that such increased surface area between the absorber and HTL/ETL does not significantly impact these results. The comparison between the 3D simulations based on the semi-prolate structure and the 1D simulation of flat surfaces show that the increased interface area has only little impact on V_{OC}, while the different generation profiles have none at all. Hence, it can be argued that the optical improvements achieved by the devices far outweigh the increased surface area.

The results here presented invite the experimental validation of these novel promising concepts. In that respect, recently F. Wang et al. [69] developed an isopropanol-assisted recrystallizing treatment for the perovskite. This method allows a practically conformal (pinholes-free) coating of the PSC layers onto

photonic-textured glass substrates with micron-sized surface features having high aspect-ratio, identical to those considered in this work. With this conformal deposition, the authors reached 18.6% PCE for a ~300 nm thick perovskite and demonstrate that it is possible to overcome the trade-off between the optical enhancements and electrical deterioration caused by structured curvatures, thereby enabling the full exploitation of the maximum optical gains.

Table 1: Main parameters attained by the electrical analysis performed in this sub-section to explore the effects of model dimensionality (3D vs. 1D simulations), the spatial distribution of photo-generation (inhomogeneous vs. homogeneous *G* profiles) and SRH recombination, for the optimized LT-structured PSCs with superstrate configuration, 300 nm perovskite thickness and Au rear contact.

Description			Jsc	Voc	FF	PCE
Dimension	**Generation**	**Recombination**	**(mA/cm²)**	**(V)**	**(%)**	**(%)**
1D	**Homogeneous** $G(z) = \langle G \rangle$	**no SRH**	27.06	1.3234	84.05	30.1
1D	**Inhomogeneous** $G(z)$	**no SRH**	26.78	1.3232	84.11	29.8
1D	**Homogeneous** $G(z) = \langle G \rangle$	**with SRH**	27.06	1.2153	81.31	26.74
1D	**Inhomogeneous** $G(z)$	**with SRH**	26.78	1.2152	81.37	26.47
3D	**Homogeneous** $G(x,y,z) = \langle G \rangle$	**no SRH**	27.28	1.3234	84.00	30.32
3D	**Inhomogeneous** $G(x,y,z)$	**no SRH**	27.09	1.3232	84.04	30.13
3D	**Homogeneous** $G(x,y,z) = \langle G \rangle$	**with SRH**	27.28	1.2106	81.32	26.85
3D	**Inhomogeneous** $G(x,y,z)$	**with SRH**	27.09	1.2104	81.35	26.68

4. Conclusions

The PSC technology has evolved to the point that optical strategies (e.g. light-trapping, LT) are becoming an indispensable solution for further efficiency improvement, as well as for bypassing the absorption losses of ultra-thin perovskite layers that benefit from improved mechanical flexibility and reduced consumption of harmful Pb.

The outcomes from this study contribute to corroborating and providing a new understanding of the underlying physical effects occurring in this emerging type of photovoltaic devices. It was shown that photonic-enhanced PSCs with ultra-thin perovskite layer (300 nm) outperform state-of-the-art planar PSCs with conventionally thicker perovskite layer (500 nm) by a significant margin (25.4% PCE enhancement). It is also demonstrated that the ultra-thin photonic-enhanced PSCs can realistically reach remarkable 26.7% PCE

values considering electronic properties similar to those of the state-of-the-art PSCs, which is below but rather close to the Shockley–Queisser limit [70].

From an optical standpoint, the less-reflective (although inexpensive) Ni rear metal contact also showed higher photocurrent for photonic-structured PSCs compared to the planar PSCs with Au or Ag.

Nonetheless, of particular interest for any application of photonic solutions in PSCs, are the full device modelling studies developed here that help understand how light trapping can influence the electrical device performance. This study also unveils how the PV performance is practically independent of the type of field distribution (homogeneous/inhomogeneous: regular/irregular) generated by the optical strategy in the perovskite absorber, as demonstrated experimentally [69]. Furthermore, 1D and 3D electrical device modelling showed almost identical solar cell performance, which will certainly motivate the PV community to simulate solar cells with ever complex geometry in a less time-consuming and straightforward way, without significantly compromising accuracy.

In another remark, although carrier recombination effects can significantly reduce the performance of PSCs, the increase in surface recombination arising from the higher surface area of the photonic structures is more than compensated from the photocurrent gain; further supporting the case towards the adoption of high efficiency and flexible PSCs fusing LT structuring. Moreover, this also indicates that the prospective design of powerful optical strategies for PSCs should primarily focus on the optimization of the broadband absorption in the perovskite material via industrially-viable LT designs, without imposing electrical-based constraints that restrict the photonic domains.

Prospectively, the LT structures investigated here can also be straightforwardly applied to tandem devices (e.g. perovskite as top cell with low-bandgap perovskite or c-Si as a sub-cell) [71–74] using adapted dimensions for maximum PV performance, while also ensuring the current matching of the sub-cells in series connection.

In summary, this work constitutes an unprecedented step for the rigorous modelling of PSCs, contributing to the development of accurate simulation tools that can be of great use by the PV industry - where the prediction of the full optoelectronic response of the devices is of extreme importance. Besides, the build-up of tools to import and simulate arbitrary device geometries and generation profiles opens new pathways to investigate novel design concepts.

Supporting Information

The Supplementary Material (SM) file includes the procedural details and presentation plus discussion of additional results concerning the optical FDTD and electrical FEM modelling studies, including the comparison with experimental device results.

Acknowledgements

This project has received funding from the European Union's Horizon 2020 research and innovation programme under the project APOLO (H2020-LCE-2017-RES-RIA), grant agreement No. 763989, and Synergy (H2020-Widespread-2020-5, CSA), grant agreement No. 952169. This publication reflects only the author's views and the European Union is not liable for any use that may be made of the information contained therein.

The work was also financed by national funds from FCT, I.P., in the scope of the projects LA/P/0037/2020, UIDP/50025/2020 and UIDB/50025/2020 of the Associate Laboratory Institute of Nanostructures, Nanomodelling and Nanofabrication – i3N, and of the projects UIDB/50011/2020 and UIDP/50011/2020 of CICECO-Aveiro Institute of Materials; as well as the FCT, I.P. projects SUPERSOLAR (PTDC/NAN-OPT/28430/2017), TACIT (PTDC/NAN-OPT/28837/2017) and FlexSolar (PTDC/CTM-REF/1008/2020).

S. Haque acknowledges the support from FCT, I.P. through the AdvaMTech PhD program scholarship PD/BD/143031/2018. M. Alexandre also acknowledges the support from FCT. I.P. through the PhD scholarship grant SFRH/BD/148078/2019. C. Baretzky and U. Würfel acknowledge the support from the Deutsche Forschungsgemeinschaft (DFG, German Research Foundation) within the priority program 2196 under project number 423746744.

Funding Sources: European Commission, FCT I.P. (Portuguese Research Foundation) and DFG (German Research Foundation).

Disclosures: The authors declare no conflicts of interest.

References

(1) Kim, J. Y.; Lee, J.-W.; Jung, H. S.; Shin, H.; Park, N.-G. High-Efficiency Perovskite Solar Cells. *Chem. Rev.* **2020**, *120* (15), 7867–7918. https://doi.org/10.1021/ACS.CHEMREV.0C00107.

(2) *Best Research-Cell Efficiency Chart | Photovoltaic Research | NREL*. https://www.nrel.gov/pv/cell-efficiency.html (accessed 2022-06-12).

(3) Yang, G.; Ren, Z.; Liu, K.; Qin, M.; Deng, W.; Zhang, H.; Wang, H.; Liang, J.; Ye, F.; Liang, Q.; Yin, H.; Chen, Y.; Zhuang, Y.; Li, S.; Gao, B.; Wang, J.; Shi, T.; Wang, X.; Lu, X.; Wu, H.; Hou, J.; Lei, D.; So, S. K.; Yang, Y.; Fang, G.; Li, G. Stable and Low-Photovoltage-Loss Perovskite Solar Cells by Multifunctional Passivation. *Nat. Photonics 2021 159* **2021**, *15* (9), 681–689. https://doi.org/10.1038/s41566-021-00829-4.

(4) Haque, S.; Alexandre, M.; Mendes, M. J.; Águas, H.; Fortunato, E.; Martins, R. Design of Wave-Optical Structured Substrates for Ultra-Thin Perovskite Solar Cells. *Appl. Mater. Today* **2020**, *20*, 100720. https://doi.org/10.1016/J.APMT.2020.100720.

(5) Saliba, M.; Matsui, T.; Seo, J.-Y.; Domanski, K.; Correa-Baena, J.-P.; Nazeeruddin, M. K.; Zakeeruddin, S. M.; Tress, W.; Abate, A.; Hagfeldt, A.; Grätzel, M. Cesium-Containing Triple Cation Perovskite Solar Cells: Improved Stability, Reproducibility and High Efficiency. *Energy Environ. Sci.* **2016**, *9* (6), 1989–1997. https://doi.org/10.1039/C5EE03874J.

(6) Kirchartz, T. Photon Management in Perovskite Solar Cells. *J. Phys. Chem. Lett.* **2019**, *10* (19), 5892–5896. https://doi.org/10.1021/ACS.JPCLETT.9B02053.

(7) Diekmann, J.; Caprioglio, P.; Futscher, M. H.; Le Corre, V. M.; Reichert, S.; Jaiser, F.; Arvind, M.; Toro, L. P.; Gutierrez-Partida, E.; Peña-Camargo, F.; Deibel, C.; Ehrler, B.; Unold, T.; Kirchartz, T.; Neher, D.; Stolterfoht, M. Pathways toward 30% Efficient Single-Junction Perovskite Solar Cells and the Role of Mobile Ions. *Sol. RRL* **2021**, *5* (8), 2100219. https://doi.org/10.1002/solr.202100219.

(8) Chung, J.; Shin, S. S.; Hwang, K.; Kim, G.; Kim, K. W.; Lee, D. S.; Kim, W.; Ma, B. S.; Kim, Y.-K.; Kim, T.-S.; Seo, J. Record-Efficiency Flexible Perovskite Solar Cell and Module Enabled by a Porous-Planar Structure as an Electron Transport Layer. *Energy Environ. Sci.* **2020**, *13* (12), 4854–4861. https://doi.org/10.1039/D0EE02164D.

(9) Zhang, J.; Zhang, W.; Cheng, H. M.; Silva, S. R. P. Critical Review of Recent Progress of Flexible Perovskite Solar Cells. *Mater. Today* **2020**, *39*, 66–88. https://doi.org/10.1016/J.MATTOD.2020.05.002.

(10) Lei, Y.; Chen, Y.; Zhang, R.; Li, Y.; Yan, Q.; Lee, S.; Yu, Y.; Tsai, H.; Choi, W.; Wang, K.; Luo, Y.; Gu, Y.; Zheng, X.; Wang, C.; Wang, C.; Hu, H.; Li, Y.; Qi, B.; Lin, M.; Zhang, Z.; Dayeh, S. A.; Pharr, M.; Fenning, D. P.; Lo, Y. H.; Luo, J.; Yang, K.; Yoo, J.; Nie, W.; Xu, S. A Fabrication Process for Flexible Single-Crystal Perovskite Devices. *Nat. 2020 5837818* **2020**, *583* (7818), 790–795. https://doi.org/10.1038/s41586-020-2526-z.

(11) Haque, S.; Mendes, M. J.; Sanchez-Sobrado, O.; Águas, H.; Fortunato, E.; Martins, R. Photonic-Structured TiO2 for High-Efficiency, Flexible and Stable Perovskite Solar Cells. *Nano Energy* **2019**, *59*, 91–101. https://doi.org/10.1016/J.NANOEN.2019.02.023.

(12) T. Vicente, A.; Araújo, A.; Mendes, M. J.; Nunes, D.; Oliveira, M. J.; Sanchez-Sobrado, O.; Ferreira, M. P.; Águas, H.; Fortunato, E.; Martins, R. Multifunctional Cellulose-Paper for Light Harvesting and Smart Sensing Applications. *J. Mater. Chem. C* **2018**, *6* (13), 3143–3181. https://doi.org/10.1039/C7TC05271E.

(13) Mendes, M. J.; Haque, S.; Sanchez-Sobrado, O.; Araújo, A.; Águas, H.; Fortunato, E.; Martins, R. Optimal-Enhanced Solar Cell Ultra-Thinning with Broadband Nanophotonic Light Capture. *iScience* **2018**, *3*, 238–254. https://doi.org/10.1016/j.isci.2018.04.018.

(14) Salomé, P. M. P.; Vermang, B.; Ribeiro-Andrade, R.; Teixeira, J. P.; Cunha, J. M. V.; Mendes, M. J.; Haque, S.; Borme, J.; Águas, H.; Fortunato, E.; Martins, R.; González, J. C.; Leitão, J. P.; Fernandes, P. A.; Edoff, M.; Sadewasser, S. Passivation of Interfaces in Thin Film Solar Cells: Understanding the Effects of a Nanostructured Rear Point Contact Layer. *Adv. Mater. Interfaces* **2018**, *5* (2), 1701101. https://doi.org/10.1002/admi.201701101.

(15) Smith, B. L.; Woodhouse, M.; Horowitz, K. A. W.; Silverman, T. J.; Zuboy, J.; Margolis, R. M. Photovoltaic (PV) Module Technologies: 2020 Benchmark Costs and Technology Evolution Framework Results. *NREL Rep.* **2021**. https://doi.org/10.2172/1829459.

(16) Mendes, M. J.; Araújo, A.; Vicente, A.; Águas, H.; Ferreira, I.; Fortunato, E.; Martins, R. Design of Optimized Wave-Optical Spheroidal Nanostructures for Photonic-Enhanced Solar Cells. *Nano Energy* **2016**, *26*, 286–296. https://doi.org/10.1016/J.NANOEN.2016.05.038.

(17) Chen, C.; Zheng, S.; Song, H.; Cong Chen; Shijian Zheng; Hongwei Song. Photon Management to Reduce Energy Loss in Perovskite Solar Cells. *Chem. Soc. Rev.* **2021**, *50* (12), 7250–7329. https://doi.org/10.1039/D0CS01488E.

(18) Alexandre, M.; Chapa, M.; Haque, S.; Mendes, M. J.; Águas, H.; Fortunato, E.; Martins, R. Optimum Luminescent Down-Shifting Properties for High Efficiency and Stable Perovskite Solar Cells. *ACS Appl. Energy Mater.* **2019**, *2* (4), 2930–2938. https://doi.org/10.1021/acsaem.9b00271.

(19) Wang, Y.; Wang, P.; Zhou, X.; Li, C.; Li, H.; Hu, X.; Li, F.; Liu, X.; Li, M.; Song, Y. Diffraction-Grated Perovskite Induced Highly Efficient Solar Cells through Nanophotonic Light Trapping. *Adv. Energy Mater.* **2018**, *8* (12). https://doi.org/10.1002/AENM.201702960.

(20) Chesman, A. S. R.; Jumabekov, A. N.; Bacal, D. M.; Lu, J.; Lal, N. N.; Hou, Q.; Bach, U.; Hu, Y.; Hou, Q.; Hu, Y.; Lu, J.; Chesman, A. S. R.; Chesman, A. S. R.; Chesman, A. S. R.; Bach, U.; Bach, U.; Bach, U. Solution-Processed Antireflective Coating for Back-Contact Perovskite Solar Cells. *Opt. Express, Vol. 28, Issue 9, pp. 12650-12660* **2020**, *28* (9), 12650–12660. https://doi.org/10.1364/OE.384039.

(21) Kwak, H.; Park, H. J.; Kim, H.; Jung, I.; Kim, J.; Lee, K.-T.; Kim, M. S.; Park, H. J.; Lee, K.-T.; Lee, K.-T. Light Absorption Enhancement in Ultrathin Perovskite Solar Cells Using Light Scattering of High-Index Dielectric Nanospheres. *Opt. Express, Vol. 29, Issue 22, pp. 35366-35376* **2021**, *29* (22), 35366–35376. https://doi.org/10.1364/OE.440989.

(22) Kang, S. M.; Jang, S.; Lee, J.-K.; Yoon, J.; Yoo, D.-E.; Lee, J.-W.; Choi, M.; Park, N.-G. Moth-Eye TiO_2 Layer for Improving Light Harvesting Efficiency in Perovskite Solar Cells. *Small* **2016**, *12* (18), 2443–2449. https://doi.org/10.1002/smll.201600428.

(23) Schmager, R.; Gomard, G.; Richards, B. S.; Paetzold, U. W. Nanophotonic Perovskite Layers for Enhanced Current Generation and Mitigation of Lead in Perovskite Solar Cells. *Sol. Energy Mater. Sol. Cells* **2019**, *192*, 65–71. https://doi.org/10.1016/J.SOLMAT.2018.12.012.

(24) Deng, K.; Liu, Z.; Wang, M.; Li, L. Nanoimprinted Grating-Embedded Perovskite Solar Cells with Improved Light Management. *Adv. Funct. Mater.* **2019**, *29* (19). https://doi.org/10.1002/ADFM.201900830.

(25) Thangavel, N. R.; Adhyaksa, G. W. P.; Dewi, H. A.; Tjahjana, L.; Bruno, A.; Birowosuto, M. D.; Wang, H.; Mathews, N.; Mhaisalkar, S. Disordered Polymer Antireflective Coating for Improved Perovskite Photovoltaics. *ACS Photonics* **2020**, *7* (8), 1971–1977. https://doi.org/10.1021/ACSPHOTONICS.0C00805.

(26) R. Erwin, W.; F. Zarick, H.; M. Talbert, E.; Rizia Bardhan. Light Trapping in Mesoporous Solar Cells with Plasmonic Nanostructures. *Energy Environ. Sci.* **2016**, *9* (5), 1577–1601. https://doi.org/10.1039/C5EE03847B.

(27) Deceglie, M. G.; Ferry, V. E.; Alivisatos, A. P.; Atwater, H. A. Design of Nanostructured Solar Cells Using Coupled Optical and Electrical Modeling. *Nano Lett.* **2012**, *12* (6), 2894–2900. https://doi.org/10.1021/nl300483y.

(28) Rahmany, S.; Etgar, L. Semitransparent Perovskite Solar Cells. *ACS Energy Lett.* **2020**, *5* (5), 1519–1531. https://doi.org/10.1021/ACSENERGYLETT.0C00417.

(29) Shahiduzzaman, M.; Hossain, M. I.; Visal, S.; Kaneko, T.; Qarony, W.; Umezu, S.; Tomita, K.; Iwamori, S.; Knipp, D.; Tsang, Y. H.; Akhtaruzzaman, M.; Nunzi, J. M.; Taima, T.; Isomura, M. Spray Pyrolyzed TiO2 Embedded Multi-Layer Front Contact Design for High-Efficiency Perovskite Solar Cells. *Nano-Micro Lett.* **2021**, *13* (1), 1–17. https://doi.org/10.1007/S40820-020-00559-2/TABLES/4.

(30) Warren, E. L.; Mcmahon, W. E.; Rienäcker, M.; Vansant, K. T.; Whitehead, R. C.; Peibst, R.; Tamboli, A. C. A Taxonomy for Three-Terminal Tandem Solar Cells. *ACS Energy Lett.* **2020**, *5* (4), 1233–1242.

https://doi.org/10.1021/ACSENERGYLETT.0C00068/SUPPL_FILE/NZ0C00068_SI_001.PDF.

(31) Geisz, J. F.; McMahon, W. E.; Buencuerpo, J.; Young, M. S.; Rienäcker, M.; Tamboli, A. C.; Warren, E. L. Characterization of Multiterminal Tandem Photovoltaic Devices and Their Subcell Coupling. *Cell Reports Phys. Sci.* **2021**, *2* (12), 100677. https://doi.org/10.1016/J.XCRP.2021.100677.

(32) Hou, Y.; Aydin, E.; De Bastiani, M.; Xiao, C.; Isikgor, F. H.; Xue, D. J.; Chen, B.; Chen, H.; Bahrami, B.; Chowdhury, A. H.; Johnston, A.; Baek, S. W.; Huang, Z.; Wei, M.; Dong, Y.; Troughton, J.; Jalmood, R.; Mirabelli, A. J.; Allen, T. G.; Van Kerschaver, E.; Saidaminov, M. I.; Baran, D.; Qiao, Q.; Zhu, K.; De Wolf, S.; Sargent, E. H. Efficient Tandem Solar Cells with Solution-Processed Perovskite on Textured Crystalline Silicon. *Science (80-.).* **2020**, *367* (6482), 1135–1140. https://doi.org/10.1126/SCIENCE.AAY0262.

(33) Chen, B.; Yu, Z. J.; Manzoor, S.; Wang, S.; Weigand, W.; Yu, Z.; Yang, G.; Ni, Z.; Dai, X.; Holman, Z. C.; Huang, J. Blade-Coated Perovskites on Textured Silicon for 26%-Efficient Monolithic Perovskite/Silicon Tandem Solar Cells. *Joule* **2020**, *4* (4), 850–864. https://doi.org/10.1016/J.JOULE.2020.01.008.

(34) Yang, T. C. J.; Fiala, P.; Jeangros, Q.; Ballif, C. High-Bandgap Perovskite Materials for Multijunction Solar Cells. *Joule* **2018**, *2* (8), 1421–1436. https://doi.org/10.1016/J.JOULE.2018.05.008.

(35) Werner, J.; Sahli, F.; Fu, F.; Diaz Leon, J. J.; Walter, A.; Kamino, B. A.; Niesen, B.; Nicolay, S.; Jeangros, Q.; Ballif, C. Perovskite/Perovskite/Silicon Monolithic Triple-Junction Solar Cells with a Fully Textured Design. *ACS Energy Lett.* **2018**, *3* (9), 2052–2058. https://doi.org/10.1021/acsenergylett.8b01165.

(36) France, R. M.; Geisz, J. F.; Song, T.; Olavarria, W.; Young, M.; Kibbler, A.; Steiner, M. A. Triple-Junction Solar Cells with 39.5% Terrestrial and 34.2% Space Efficiency Enabled by Thick Quantum Well Superlattices. *Joule* **2022**, *6* (5), 1121–1135. https://doi.org/10.1016/J.JOULE.2022.04.024.

(37) *Nanophotonic FDTD Simulation Software - Lumerical FDTD*. https://www.lumerical.com/products/fdtd/ (accessed 2022-06-12).

(38) *tiberCAD | DEVELOPER COMMUNITY*. http://www.tibercad.org/ (accessed 2022-06-12).

(39) *CHARGE solver introduction – Lumerical Support*. https://support.lumerical.com/hc/en-us/articles/360034917693-CHARGE-solver-introduction (accessed 2022-06-12).

(40) *Sentaurus Device - Technology Computer Aided Design (TCAD) | Synopsys*. https://www.synopsys.com/silicon/tcad/device-simulation/sentaurus-device.html (accessed 2022-06-12).

(41) Chapa, M.; Alexandre, M. F.; Mendes, M. J.; Águas, H.; Fortunato, E.; Martins, R. All-Thin-Film Perovskite/C–Si Four-Terminal Tandems: Interlayer and Intermediate Contacts Optimization. *ACS Appl. Energy Mater.* **2019**, *2* (6), 3979–3985. https://doi.org/10.1021/acsaem.9b00354.

(42) Adhyaksa, G. W. P.; Johlin, E.; Garnett, E. C. Nanoscale Back Contact Perovskite Solar Cell Design for Improved Tandem Efficiency. *Nano Lett.* **2017**, *17* (9), 5206–5212. https://doi.org/10.1021/acs.nanolett.7b01092.

(43) Sanchez-Sobrado, O.; Mendes, M. J.; Haque, S.; Mateus, T.; Araujo, A.; Aguas, H.; Fortunato, E.; Martins, R. Colloidal-Lithographed TiO_2 Photonic Nanostructures for Solar Cell Light Trapping. *J. Mater. Chem. C* **2017**, *5* (27), 6852–6861. https://doi.org/10.1039/C7TC01756A.

(44) Centeno, P.; Alexandre, M. F.; Chapa, M.; Pinto, J. V.; Deuermeier, J.; Mateus, T.; Fortunato, E.; Martins, R.; Águas, H.; Mendes, M. J. Self-Cleaned Photonic-Enhanced Solar Cells with Nanostructured Parylene-C. *Adv. Mater. Interfaces* **2020**, *7* (15), 2000264. https://doi.org/10.1002/ADMI.202000264.

(45) Boane, J. L. N.; Centeno, P.; Mouquinho, A.; Alexandre, M.; Calmeiro, T.; Fortunato, E.; Martins, R.; Mendes, M. J.; Águas, H. Soft-Microstructured Transparent Electrodes for Photonic-Enhanced Flexible Solar Cells. *Micro 2021, Vol. 1, Pages 215-227* **2021**, *1* (2), 215–227. https://doi.org/10.3390/MICRO1020016.

(46) Oliveira, R. D.; Mouquinho, A.; Centeno, P.; Alexandre, M.; Haque, S.; Martins, R.; Fortunato, E.; Águas, H.; Mendes, M. J. Colloidal Lithography for Photovoltaics: An Attractive Route for Light Management. *Nanomater. 2021, Vol. 11, Page 1665* **2021**, *11* (7), 1665. https://doi.org/10.3390/NANO11071665.

(47) Sanchez-Sobrado, O.; Mendes, M. J.; Haque, S.; Mateus, T.; Aguas, H.; Fortunato, E.; Martins, R. Lightwave Trapping in Thin Film Solar Cells with Improved Photonic-Structured Front Contacts. *J. Mater. Chem. C* **2019**, *7* (21), 6456–6464. https://doi.org/10.1039/C8TC06092D.

(48) Sanchez-Sobrado, O.; Mendes, M. J.; Mateus, T.; Costa, J.; Nunes, D.; Aguas, H.; Fortunato, E.; Martins, R. Photonic-Structured TCO Front Contacts Yielding Optical and Electrically Enhanced Thin-Film Solar Cells. *Sol. Energy* **2020**, *196*, 92–98. https://doi.org/10.1016/J.SOLENER.2019.11.051.

(49) Yang, D.; Yang, R.; Priya, S.; Liu, S. F. Recent Advances in Flexible Perovskite Solar Cells: Fabrication and Applications. *Angew. Chemie Int. Ed.* **2019**, *58* (14), 4466–4483. https://doi.org/10.1002/anie.201809781.

(50) He, R.; Nie, S.; Huang, X.; Wu, Y.; Chen, R.; Yin, J.; Wu, B.; Li, J.; Zheng, N. Scalable Preparation of High-Performance ZnO–SnO2 Cascaded Electron Transport Layer for Efficient Perovskite Solar Modules. *Sol. RRL* **2021**, 2100639. https://doi.org/10.1002/SOLR.202100639.

(51) Li, R.; Wang, P.; Chen, B.; Cui, X.; Ding, Y.; Li, Y.; Zhang, D.; Zhao, Y.; Zhang, X. NiOx/Spiro Hole Transport Bilayers for Stable Perovskite Solar Cells with Efficiency Exceeding 21%. *ACS Energy Lett.* **2020**, *5* (1), 79–86. https://doi.org/10.1021/ACSENERGYLETT.9B02112/SUPPL_FILE/NZ9B02112_SI_001.PDF.

(52) Chen, Z.; Li, W.; Li, R.; Zhang, Y.; Xu, G.; Cheng, H. Fabrication of Highly Transparent and Conductive Indium-Tin Oxide Thin Films with a High Figure of Merit via Solution Processing. *Langmuir* **2013**, *29* (45), 13836–13842. https://doi.org/10.1021/LA4033282/SUPPL_FILE/LA4033282_SI_001.PDF.

(53) Pang, S.; Zhang, C.; Dong, H.; Chen, D.; Zhu, W.; Xi, H.; Chang, J.; Lin, Z.; Zhang, J.; Hao, Y. Efficient NiO x Hole Transporting Layer Obtained by the Oxidation of Metal Nickel Film for Perovskite Solar Cells. *ACS Appl. Energy Mater.* **2019**, *2* (7), 4700–4707. https://doi.org/10.1021/ACSAEM.9B00169/SUPPL_FILE/AE9B00169_SI_001.PDF.

(54) Hossain, M. I.; Shahiduzzaman, M.; Ahmed, S.; Huqe, M. R.; Qarony, W.; Saleque, A. M.; Akhtaruzzaman, M.; Knipp, D.; Tsang, Y. H.; Taima, T.; Zapien, J. A. Near Field Control for Enhanced Photovoltaic Performance and Photostability in Perovskite Solar Cells. *Nano Energy* **2021**, *89*, 106388. https://doi.org/10.1016/J.NANOEN.2021.106388.

(55) Piprek, J. HANDBOOK OF OPTOELECTRONIC DEVICE MODELING AND SIMULATION : Lasers. *CRC Press* **2021**. https://doi.org/10.4324/9781315152318.

(56) Patel, P. K. Device Simulation of Highly Efficient Eco-Friendly CH3NH3SnI3 Perovskite Solar Cell. *Sci. Reports 2021 111* **2021**, *11* (1), 1–11. https://doi.org/10.1038/s41598-021-82817-w.

(57) Liu, P.; Wang, W.; Liu, S.; Yang, H.; Shao, Z.; Liu, P.; Wang, W.; Liu, S.; Shao, Z.; Yang, H. Fundamental Understanding of Photocurrent Hysteresis in Perovskite Solar Cells. *Adv. Energy Mater.* **2019**, *9* (13), 1803017. https://doi.org/10.1002/AENM.201803017.

(58) Létay, G.; Hermle, M.; Bett, A. W. Simulating Single-Junction GaAs Solar Cells Including Photon Recycling. *Prog. Photovoltaics Res. Appl.* **2006**, *14* (8), 683–696. https://doi.org/10.1002/PIP.699.

(59) Burke, T. M.; Sweetnam, S.; Vandewal, K.; McGehee, M. D.; Burke, T. M.; Sweetnam, S.; McGehee, M. D.; Vandewal, K. Beyond Langevin Recombination: How Equilibrium Between Free Carriers and Charge Transfer States Determines the Open-Circuit Voltage of Organic Solar Cells. *Adv. Energy Mater.* **2015**, *5* (11), 1500123. https://doi.org/10.1002/AENM.201500123.

(60) Huang, L.; Cui, X.; Liu, C.; Yang, W.; Shi, W.; Lai, J.; Wang, L. Improvement on Performance of Hybrid CH3NH3PbI3−xClx Perovskite Solar Cells Induced Sequential Deposition by Low Pressure Assisted Solution Processing. *Sol. Energy* **2020**, *199*, 826–831. https://doi.org/10.1016/J.SOLENER.2020.02.080.

(61) Budiawan, W.; Lai, K. W.; Karuppuswamy, P.; Jadhav, T. S.; Lu, Y. A.; Ho, K. C.; Wang, P. C.; Chang, C. C.; Chu, C. W. Asymmetric Benzotrithiophene-Based Hole Transporting Materials Provide High-Efficiency Perovskite Solar Cells. *ACS Appl. Mater. Interfaces* **2020**, *12* (26), 29143–29152. https://doi.org/10.1021/ACSAMI.0C02204/SUPPL_FILE/AM0C02204_SI_001.PDF.

(62) Geffroy, C.; Grana, E.; Bessho, T.; Almosni, S.; Tang, Z.; Sharma, A.; Kinoshita, T.; Awai, F.; Cloutet, E.; Toupance, T.; Segawa, H.; Hadziioannou, G. P-Doping of a Hole Transport Material via a Poly(Ionic Liquid) for over 20% Efficiency and Hysteresis-Free Perovskite Solar Cells. *ACS Appl. Energy Mater.* **2020**, *3* (2), 1393–1401. https://doi.org/10.1021/ACSAEM.9B01819/SUPPL_FILE/AE9B01819_SI_001.PDF.

(63) Kirchartz, T.; Krückemeier, L.; Unger, E. L. Research Update: Recombination and Open-Circuit Voltage in Lead-Halide Perovskites. *APL Mater.* **2018**, *6* (10), 100702. https://doi.org/10.1063/1.5052164.

(64) Crothers, T. W.; Milot, R. L.; Patel, J. B.; Parrott, E. S.; Schlipf, J.; Müller-Buschbaum, P.; Johnston, M. B.; Herz, L. M. Photon Reabsorption Masks Intrinsic Bimolecular Charge-Carrier Recombination in CH3NH3PbI3 Perovskite. *Nano Lett.* **2017**, *17* (9), 5782–5789. https://doi.org/10.1021/ACS.NANOLETT.7B02834/SUPPL_FILE/NL7B02834_SI_001.PDF.

(65) Green, M. A.; Dunlop, E. D.; Hohl-Ebinger, J.; Yoshita, M.; Kopidakis, N.; Ho-Baillie, A. W. Y. Solar Cell Efficiency Tables (Version 55). *Prog. Photovoltaics Res. Appl.* **2020**, *28* (1), 3–15. https://doi.org/10.1002/PIP.3228.

(66) Bertoluzzi, L.; Boyd, C. C.; Rolston, N.; Xu, J.; Prasanna, R.; O'Regan, B. C.; McGehee, M. D. Mobile Ion Concentration Measurement and Open-Access Band Diagram Simulation Platform for Halide Perovskite Solar Cells. *Joule* **2020**, *4* (1), 109–127. https://doi.org/10.1016/J.JOULE.2019.10.003.

(67) Walter, D.; Fell, A.; Wu, Y.; Duong, T.; Barugkin, C.; Wu, N.; White, T.; Weber, K. Transient Photovoltage in Perovskite Solar Cells: Interaction of Trap-Mediated Recombination and Migration of Multiple Ionic Species. *J. Phys. Chem. C* **2018**, *122* (21), 11270–11281. https://doi.org/10.1021/ACS.JPCC.8B02529/SUPPL_FILE/JP8B02529_SI_001.PDF.

(68) Stolterfoht, M.; Caprioglio, P.; Wolff, C. M.; Márquez, J. A.; Nordmann, J.; Zhang, S.; Rothhardt, D.; Hörmann, U.; Amir, Y.; Redinger, A.; Kegelmann, L.; Zu, F.; Albrecht, S.; Koch, N.; Kirchartz, T.; Saliba, M.; Unold, T.; Neher, D. The Impact of Energy Alignment and Interfacial Recombination on the Internal and External Open-Circuit Voltage of Perovskite Solar Cells. *Energy Environ. Sci.* **2019**, *12* (9), 2778–2788. https://doi.org/10.1039/C9EE02020A.

(69) Wang, F.; Zhang, Y.; Yang, M.; Fan, L.; Yang, L.; Sui, Y.; Yang, J.; Zhang, X. Toward Ultra-Thin and Omnidirectional Perovskite Solar Cells: Concurrent Improvement in Conversion Efficiency by Employing Light-Trapping and Recrystallizing Treatment. *Nano Energy* **2019**, *60*, 198–204. https://doi.org/10.1016/j.nanoen.2019.03.059.

(70) Rühle, S. Tabulated Values of the Shockley–Queisser Limit for Single Junction Solar Cells. *Sol. Energy* **2016**, *130*, 139–147. https://doi.org/10.1016/J.SOLENER.2016.02.015.

(71) Qarony, W.; Hossain, M. I.; Salleo, A.; Knipp, D.; Tsang, Y. H. Rough versus Planar Interfaces:

How to Maximize the Short Circuit Current of Perovskite Single and Tandem Solar Cells. *Mater. Today Energy* **2019**, *11*, 106–113. https://doi.org/10.1016/J.MTENER.2018.10.001.

(72) Hossain, M. I.; Qarony, W.; Ma, S.; Zeng, L.; Knipp, D.; Tsang, Y. H. Perovskite/Silicon Tandem Solar Cells: From Detailed Balance Limit Calculations to Photon Management. *Nano-Micro Lett. 2019 111* **2019**, *11* (1), 1–24. https://doi.org/10.1007/S40820-019-0287-8.

(73) Hossain, M. I.; Shahiduzzaman, M.; Saleque, A. M.; Huqe, M. R.; Qarony, W.; Ahmed, S.; Akhtaruzzaman, M.; Knipp, D.; Tsang, Y. H.; Taima, T.; Zapien, J. A. Improved Nanophotonic Front Contact Design for High-Performance Perovskite Single-Junction and Perovskite/Perovskite Tandem Solar Cells. *Sol. RRL* **2021**, *5* (10), 2100509. https://doi.org/10.1002/SOLR.202100509.

(74) Hossain, M. I.; Qarony, W.; Jovanov, V.; Tsang, Y. H.; Knipp, D. Nanophotonic Design of Perovskite/Silicon Tandem Solar Cells. *J. Mater. Chem. A* **2018**, *6* (8), 3625–3633. https://doi.org/10.1039/C8TA00628H.

Supplementary Material

Photonic-Structured Perovskite Solar Cells: Detailed Optoelectronic Analysis

Sirazul Haque[1,2,*], Miguel Alexandre[1], Clemens Baretzky[3,4], Daniele Rossi[5], Francesca De Rossi[5], António T. Vicente[1], Francesca Brunetti[5], Hugo Águas[1], Rute A. S. Ferreira[2], Elvira Fortunato[1], Matthias Auf der Maur[5], Uli Würfel[3,4], Rodrigo Martins[1], Manuel J. Mendes[1,*]

[1] *CENIMAT|i3N, Department of Materials Science, School of Science and Technology, NOVA University of Lisbon and CEMOP/UNINOVA, Campus de Caparica, 2829-516 Caparica, Portugal*

[2] *Department of Physics, CICECO - Aveiro Institute of Materials, University of Aveiro, Campus Universitário de Santiago, 3810-193 Aveiro, Portugal*

[3] *Fraunhofer Institute for Solar Energy Systems ISE, Heidenhofstr. 2, 79110 Freiburg, Germany*

[4] *Freiburg Material Research Center FMF, University of Freiburg, Stefan-Meier-Str. 21, 79104 Freiburg, Germany*

[5] *CHOSE, Department of Electronic Engineering, Università degli Studi di Roma Tor Vergata, Via del Politecnico 1, 00133 Rome, Italy*

**Corresponding authors: s.haque@campus.fct.unl.pt, mj.mendes@fct.unl.pt*

S1. Electromagnetic FDTD simulation process and setup

The superstrate-type and substrate-type PSC architectures of Figure 1,a are composed of 5 layers conformally coated onto micro-structured transparent substrates, which are compared to reference planar (non-structured) cells composed of the same layers. The optical response of the materials is determined by their complex refractive index ($N=n+ik$) spectra, which were taken from published experimental data and are presented in Figure S1. The perovskite absorber material considered in this work is methylammonium lead iodide, $MAPbI_3$, taking a widely-used refractive index function fitted from measured values provided by Phillips *et al.*, available in a common database [1,2]. However, it should be pointed out that, contrarily to other more matured PV technologies, PSCs are still highly dependent on the specific fabrication conditions and process materials used. Therefore, there is presently no (n, k) dataset that can be taken as a technological standard. For the superstrate configuration, the refractive index of the transparent substrate was accounted for by a fixed real value, attributed to the background index of the simulation volume, equal to n=1.5 (e.g. similar to the index of PET); while for the substrate configuration a background index n=1.6 was taken to account for a typical transparent adhesive material used for encapsulation over the PSC layers.

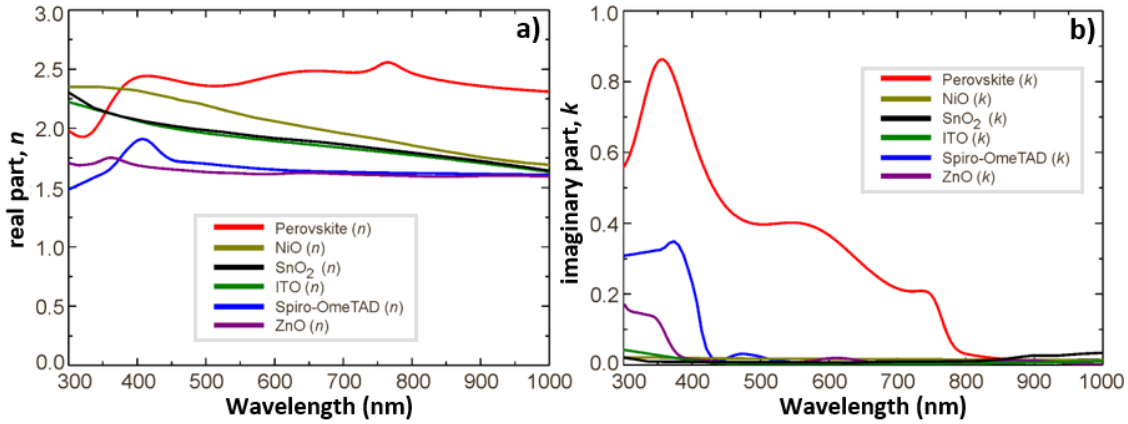

Figure. S1: Spectra of the real, n (a), and imaginary, k (b), parts of the complex refractive indices of the materials used in this work [3,4].

The photonic features patterned on the substrate are arranged in a hexagonal array (honeycomb lattice), as sketched in Figure 1,a. Therefore, the FDTD computations were carried out in a 3D unit cell, corresponding to one period of the hexagonal array. The PSCs are illuminated by a plane wave source placed in the background medium above the structures. The computational unit cell was delimitated by boundary conditions (BCs): perfect matching layers (PML) were applied in the top (above the source) and bottom (bellow the cells) planes to prevent reflections of outgoing waves, and in the lateral planes periodic BCs were set to simulate the infinite periodicity of the structure of the solar cell. At normal illumination, the symmetry of the LT elements relative to the incidence direction also allowed calculating only one quadrant

of the unit cell, employing symmetric (for the x-axis) and anti-symmetric (for the y-axis) BCs, thus reducing the computation time.

The FDTD simulations were performed with a cubic mesh design adapted to the structures, composed of spatial step sizes limited between 0.25-5 nm. The maximum physical FDTD time imposed on the simulations was 1500-2000 fs. According to extensive validation tests performed, these computational settings were revealed to be sufficient for the accurate convergence of the electromagnetic field solutions in the investigated structures [3–5]. The optical excitation is the broadband solar spectrum (AM 1.5G), and each simulation is performed for 251 wavelength (λ) points considered at equally spaced wavelengths along with the 300-1000 nm source wavelength range, since the AM1.5 solar photon flux outside this bandwidth is small.

We are interested in analyzing the light absorption across the PSC structure, i.e. the power absorbed per unit volume (P_{ABS}) in each element of the structures, which is given by the resulting electric field distribution established in its material:

$$P_{ABS} = \frac{1}{2}\omega\varepsilon''|\boldsymbol{E}|^2 \qquad \text{(S1)}$$

where $|\mathbf{E}|^2$ is the electric field intensity, ω is the angular frequency of the light and ε" is the imaginary part of the dielectric permittivity. P_{ABS} is normalized by the source power to obtain the absorption density (p_{ABS}, units of m^{-3}). The absorption of light for a particular wavelength (λ) is determined by integrating p_{ABS} along the absorber volume: $Abs(\lambda) = \int p_{ABS}(\lambda)dV$. The number of photons absorbed per unit volume and per unit time is the photon absorption rate: $g(\omega)=P_{ABS}/E_{PH}$; where $E_{PH}=\hbar\omega$ is the photon energy.

Here we consider that each absorbed photon excites one electron-hole pair, so g is equivalent to the optical generation rate. Since the illumination is provided by a broadband source, characterized by a spectral irradiance (instead of a power density), the E-field is substituted by an electric-field spectral density such that its intensity, $|\mathbf{E}|^2$, becomes with units of $V^2m^{-2}Hz^{-1}$. In this way, g is normalized to a spectral generation rate (in units of $m^{-3}s^{-1}Hz^{-1}$) such that the total generation rate (G, units of $m^{-3}s^{-1}$) is determined by integrating over the frequency range of the source bandwidth: $G = \int g(\omega)d\omega$ [5].

A relevant quantity evaluated was the "optical" photocurrent density (J_{PH}) which is computed considering an ideal internal quantum efficiency of the PSCs equal to 100% (i.e. every photon absorbed in the perovskite material generates carriers collected by the contacts) [3–5]. Thus, J_{PH} is determined by integrating the absorption in the perovskite, multiplied with the solar power spectrum AM1.5G ($I_{AM\,1.5}$, units of $Wm^{-2}m^{-1}$), across the chosen computation wavelength range (300-1000 nm):

$$J_{PH} = e\int \frac{\lambda}{hc} Abs(\lambda)\, I_{AM1.5}(\lambda)d\lambda \qquad \text{(S2)}$$

where *e* is the electron's charge, *h* is Planck's constant and *c* is the light velocity in vacuum. This spectrally-integrated J_{PH} creates an upper limit to the attainable short-circuit current density of the cell since it neglects any electrical losses. Furthermore, this parameter was also used in the optical simulations as the figure-of-merit to optimize the geometry of the substrate features – modelled as semi-spheroidal shapes with an axis of revolution aligned with the illumination direction.

Concerning the optimization process, a particle swarm optimization (PSO) algorithm [3,4,6,7] was used in the programs to perform a complete screening of the parameters of the light trapping (LT) structures and solar cells' layers (depicted in Figure 1,a) that yield the highest photocurrent density, J_{PH}. The algorithm iteratively adjusts the structures' geometry to maximize absorption in the perovskite material, while minimizing optical losses (i.e. total reflection and absorption occurring in front layers: ITO, SnO_2, ZnO and/or in rear contacts: Spiro-OmeTAD, NiO materials). Population-based stochastic optimization techniques as PSO are preferential when operating with complex physical systems, as in the present wave-optics regime where there is a strong correlation between all parameters [3,4,6,7], that imposes significant constraints for an accurate determination of any Figure-of-Merit by sequential parameter sweeping [3,4,6,7].

4.1 S1.1 Optical modelling results

Table S1 presents the outcome of the optimized set of geometrical parameters which produce the highest photocurrent for the cells shown in Figure 1,a. Here, *R*, R_z and *p* define the geometry of the LT structures patterned on the substrates, and the t_{layer} values represent the thickness of specific layers of the PSCs. These quantities were chosen as variables in the PSO algorithm that iteratively searched for the optimal set of parameters that maximizes J_{PH} (equation S2) produced in the perovskite material. The LT enhancement values shown in brackets for each case were calculated relative to the corresponding planar reference cell with optimized double-layer (TCO+ETL) anti-reflection coating (ARC, also shown in Table S1) but without structuring any layer as shown in Figure S3. It is important to note that lower limits for the thicknesses of the selective contact layers (i.e., t_{ITO}, t_{SnO2}, t_{Spiro}, t_{ZnO}, t_{NiO}) were applied in the PSO search domain, to align the layers' configuration with the experimental state-of-the-art and to guarantee their electrical performance.

Table S1: *Geometrical parameters of the photonic-structured PSCs that allow the maximum photocurrent (J_{PH}) determined by the optical PSO optimizations. The values of the photocurrent gain relative to the reference (planar) PSCs are indicated in brackets. R, Rz and p define the geometry of the designed LT structures patterned on the substrates, and the t values represent the thickness of specific layers. These quantities were chosen as variables in the optimization algorithm that iteratively searched for the optimal set of parameters that maximizes the photocurrent produced by the perovskite material*

Light Trapping Structures	**300 nm Perovskite layer**		**500 nm Perovskite layer**	
	Optimal Parameters	J_{PH}, mA/cm^2 (LT enhancement)	Optimal Parameters	J_{PH}, mA/cm^2 (LT enhancement)

Superstrate Configuration				
Optimized Planar PSCs with **Au** metal contact	t_{ITO} = 350 nm t_{SnO2} = 25 nm t_{Spiro} = 150 nm t_{Au} = 200 nm	**23.5**	t_{ITO} = 350 nm t_{SnO2} = 25 nm t_{Spiro} = 150 nm t_{Au} = 200 nm	**25.1**
Optimized Structured PSCs with **Au** Metal Contact	t_{ITO} = 350 nm t_{SnO2} = 25 nm t_{Spiro} = 150 nm t_{Au} = 200 nm R = 518.4 nm Rz = 627.4 nm p = 1100.6 nm	**27.2** (15.3%)	t_{ITO} = 350 nm t_{SnO2} = 25 nm t_{Spiro} = 150 nm t_{Au} = 200 nm R = 445.4 nm Rz = 669.7 nm p = 907.3 nm	**30.3** (20.7%)
Optimized Planar PSCs with **Ag** Metal Contact	t_{ITO} = 350 nm t_{SnO2} = 25 nm t_{Spiro} = 150 nm t_{Ag} = 200 nm	**23.6**	t_{ITO} = 350 nm t_{SnO2} = 25 nm t_{Spiro} = 150 nm t_{Ag} = 200 nm	**25.2**
Optimized Structured PSCs with **Ag** Metal Contact	t_{ITO} = 350 nm t_{SnO2} = 25 nm t_{Spiro} = 150 nm t_{Ag} = 200 nm R = 527.1 nm Rz = 627.4 nm p = 1096.8 nm	**27.3** 14.7%	t_{ITO} = 350 nm t_{SnO2} = 25 nm t_{Spiro} = 150 nm t_{Ag} = 200 nm R = 263.0 nm Rz = 655.4 nm p = 526.0 nm	**30.6** (21.4%)
Substrate Configuration				
Optimized Planar PSCs with **Au** Metal Contact	t_{ITO} = 350 nm t_{ZnO} = 100 nm t_{NiO} = 50 nm t_{Ni} = 200 nm	**22.6**	t_{ITO} = 350 nm t_{ZnO} = 100 nm t_{NiO} = 50 nm t_{Ni} = 200 nm	**24.6**
Optmized Structured PSCs with **Au** Metal Contact	t_{ITO} = 350 nm t_{ZnO} = 100 nm t_{NiO} = 10 nm t_{Au} = 200 nm R = 254.2 nm Rz = 662.8 nm p = 508.4 nm	**27.6** (22.1%)	t_{ITO} = 350 nm t_{ZnO} = 100 nm t_{NiO} = 10 nm t_{Au} = 200 nm R = 420.8 nm Rz = 677.1 nm p = 920.2 nm	**28.8** (14.7%)
Optimized Planar PSCs with **Ni** Metal Contact	t_{ITO} = 350 nm t_{ZnO} = 100 nm t_{NiO} = 10 nm t_{Ni} = 200 nm	**21.1**	t_{ITO} = 350 nm t_{ZnO} = 100 nm t_{NiO} = 10 nm t_{Ni} = 200 nm	**23.5**
Optmized Structured PSCs with **Ni** Metal Contact	t_{ITO} = 350 nm t_{ZnO} = 100 nm t_{NiO} = 54 nm t_{Ni} = 200 nm R = 250.0 nm Rz = 551.3 nm p = 500.0 nm	**23.2** (11.0%)	t_{ITO} = 350 nm t_{ZnO} = 100 nm t_{NiO} = 50 nm t_{Ni} = 200 nm R = 403.0 nm Rz = 678.1 nm p = 806.0 nm	**25.2** (6.3%)

Different materials were explored for the selective contacts (ETL/HTL plus metallic electrode) in each configuration, to assess distinct alternatives in view of lowering the process costs while maintaining high performance. Here, as test bed of our study the standard MAPI (methylammonium lead iodide) perovskite

was taken for the absorber material, with two different thicknesses investigated: the conventional 500 nm and an ultrathin 300 nm layer (for improved mechanical flexibility).

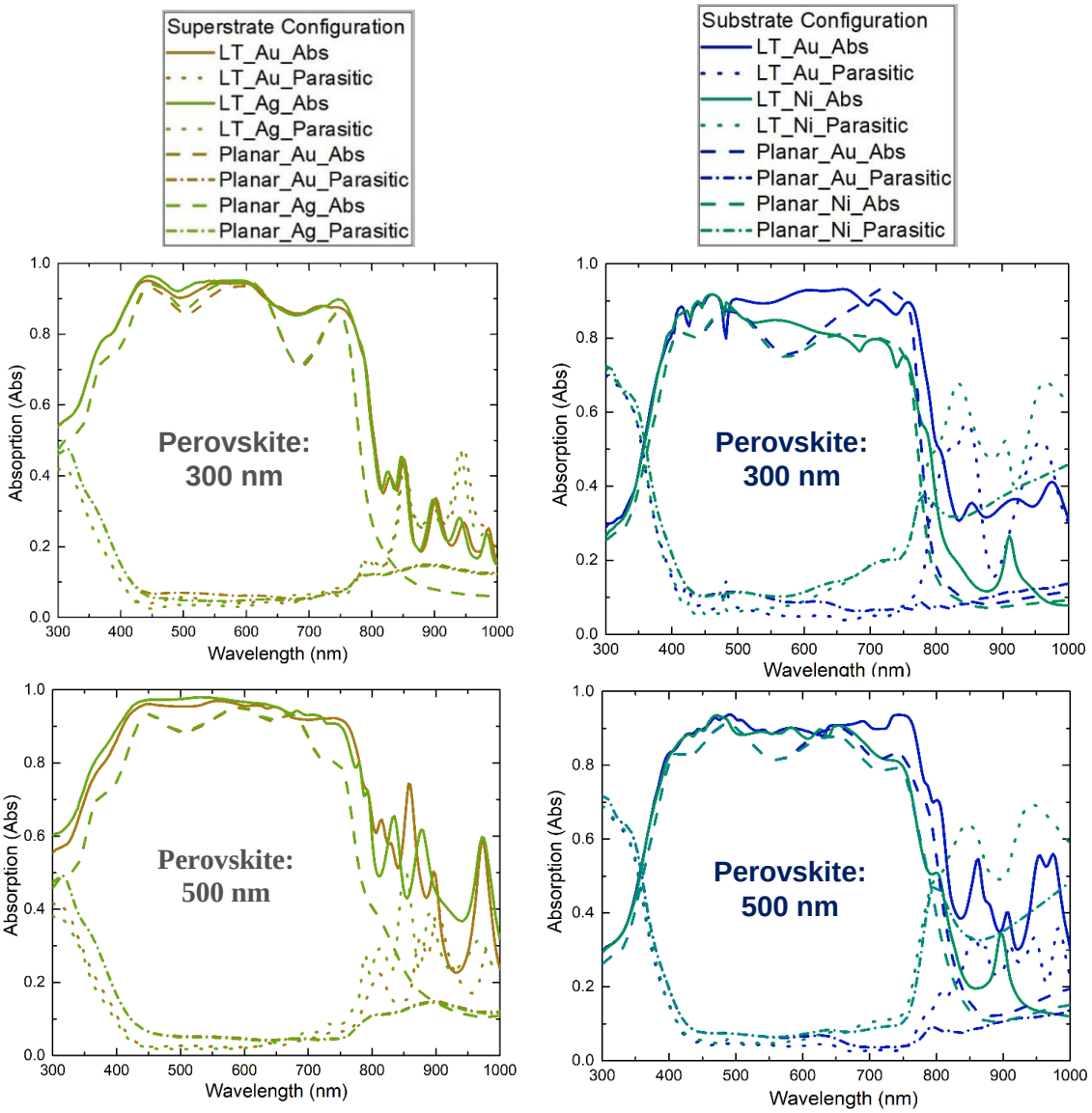

Figure. S2: Light absorption spectra of the PSCs with (LT) or without (Planar) the photonic structures, for the different cell architectures: (*left:* superstrate, *right:* substrate), for different perovskite thicknesses (*top:* 300 nm, *bottom:* 500 nm) and different metals (Au, Ag, Ni) composing the rear contact. For each case we show the absorption occurring only in the perovskite layer (Abs) and that occurring in the other layers of the devices (Parasitic).

The absorption curves for the optimized photonic-structured PSCs and their corresponding reference cells are presented in Figure S2 for the distinct perovskite thicknesses and the superstrate and substrate configurations. It is clearly shown for all cases that the photonic-enhanced cells absorb significantly higher relative to the optimized reference (planar) cells throughout the whole spectrum. The absorption gains are

attained chiefly by two optical mechanisms: anti-reflection and light scattering properties which are explained in section 3.1 of the manuscript.

On a side note concerning the spectra obtained in Figure S2, we point out that the contribution of below-bandgap photons to the cells' quantum efficiency (QE) is still a topic of intense debate in the solar cell community [8–10]. What has, however, become clear is that, depending on the particular solar cell properties, such contribution can indeed become significant. Namely, sub-bandgap QE, caused by photon absorption in the tail states, has been indisputably observed by several research groups, in PV materials such as CIGS [10] and organic semiconductors [8]. These principles should also apply to PSCs, so that the NIR light absorption seen here can be replicated in the measured QE spectra with appropriate PSC fabrication. Furthermore, very recently, it was experimentally observed that excess carriers occupying the Urbach tails (due to sub-bandgap absorption) can contribute to photocurrent generation in $MAPbI_3$ based perovskite [9], the same absorber material used in this study. As such, the sub-bandgap spectrum is accounted for in the calculations. Considering the 300 nm perovskite, it can be seen that most absorption (90-95%) occurs for wavelengths between 300-850 nm (see Figure S2) and only a small sub-bandgap absorption is observed at wavelengths between 850-1000 nm. On the other hand, the thicker 500 nm perovskite shows higher sub-bandgap gains (see Figure S2), as the increased thickness improves the far-field scattering and provides a longer photon travel path. From an electrical standpoint, absorption in such sub-bandgap spectrum has a much lower effect on PCE compared to the above-bandgap spectrum [9]. Therefore, from this analysis it is expected that the 300 nm photonic-enhanced perovskite will not only outperform the planar (500 nm) cells but will also be closely following the 500 nm photonic-enhanced device performances electrically, as observed in the electrical simulation results in section 3.2 of the manuscript.

We further elaborate on the parasitic absorption that occurs in the PSCs, which mainly takes place in the front layers (TCO, made of ITO, plus ETLs) at the shorter wavelengths (300-600 nm), as shown in the absorption curves of Figure S2 a,b and in the optical generation (G) profiles of Figure 2b and Figure S3. The photonic-structured PSCs suffer from substantially lower parasitic absorption losses in the whole UV-VIS spectrum relative to their planar counterpart references. This is mostly achieved due to better geometrical index matching caused by the front curvatures of the combined top layers and perovskite absorber, consequently rendering superior light coupling towards the absorber material with high *n* value, and avoiding its back-reflection onto the front layers (ITO+ETLs). Oppositely, it is seen that more intense parasitic absorption occurs in the longer wavelengths (>800 nm) in the photonic-structured PSCs relative to the planar references. In the planar PSCs, the NIR parasitic absorption is mainly due to the characteristic free-carrier absorption within the ITO material (with increasing *k* values in the NIR region), and additional absorption in the HTLs, as shown in Figure S3. However, for the photonic-structured cells, the main source for such optical losses in the NIR is strong plasmonic effects in the periodically-corrugated HTL/metal interfaces, as seen in Figure 2 in section 3.1. Grating-like structures are conducive to the excitation of

surface plasmon polaritons (SPP) in metal/dielectric interfaces, but not in dielectric/dielectric interfaces, since they heavily rely on a significant number of free electrons [11–17]. Thence, in the simulated devices, only the corrugated HTL/Rear Metal interface can excite SPPs. As such, and taking into account the evanescent (short-range) nature of their electric near-field profile, it is clear that SPPs do not play a direct role in the perovskite's absorption [4]. Regardless, their presence can still account for significant parasitic absorption in the overall device structure, as shown in the corrugated HTL/Rear metal interface of the optical generation (G) profiles in Figure 2b. This explanation can be further justified by comparing with an earlier study [3] addressing photonic-enhanced PSCs with flat rear metal contacts, where no SPP contribution is detected since the rear metal is planar, but similar "useful" absorption enhancement peaks were observed in the longer wavelengths, even in the absence of a corrugated metal contact.

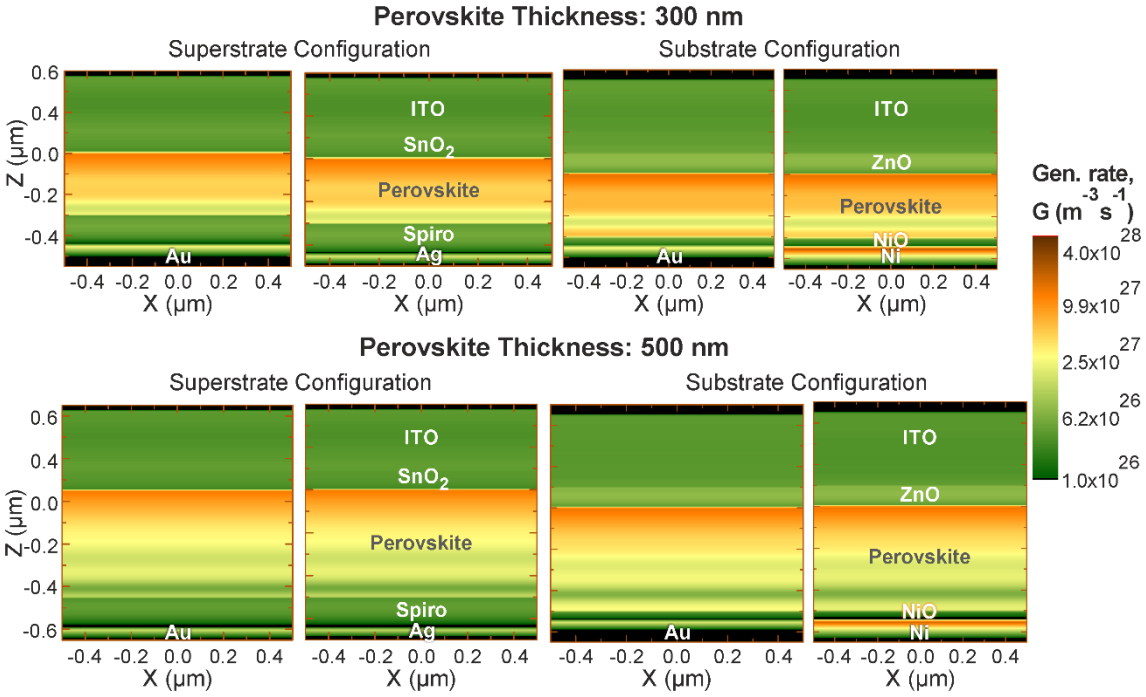

Figure. S3: The profiles represent the log-scale distribution of the total generation rate, *G*, along the *xz* cross-sectional plane of the planar cells passing by the center, respectively for the PSCs with the 300 nm (top) and 500 nm (bottom) thick perovskite absorbers in superstrate and substrate configuration with different metal contacts as indicated.

To probe the attainable performances with even thinner perovskite layers below those (300 and 500 nm) considered in this study, a final optimization was performed for the LT design considering a 150 nm thick perovskite, which can allow further improvements in flexibility and overall applicability of PSCs. These results are presented in Figure S4, which shows that the photonic structuring is also capable of pronouncedly adding absorption to the perovskite layer mainly for the longer wavelengths (>600 nm), where the ultra-thin device performance drops. Therefore, the LT-enhanced cell demonstrated an overall 22.8% photocurrent improvement with the 150 nm thick perovskite layer compared to its counterpart planar cell

(no LT), as shown in the inset of Figure S4. Such optical gain is a little higher than those reported for 300 and 500 nm perovskite absorbers (see Table S1). This is expected, as the thinner the absorber the higher can be the boost in absorption caused by effective LT, in accordance with the trend of the Lambertian formalism (predicting a relation between photocurrent gains and absorber thickness) previously presented for perovskite-based PV by the authors in ref. [3].

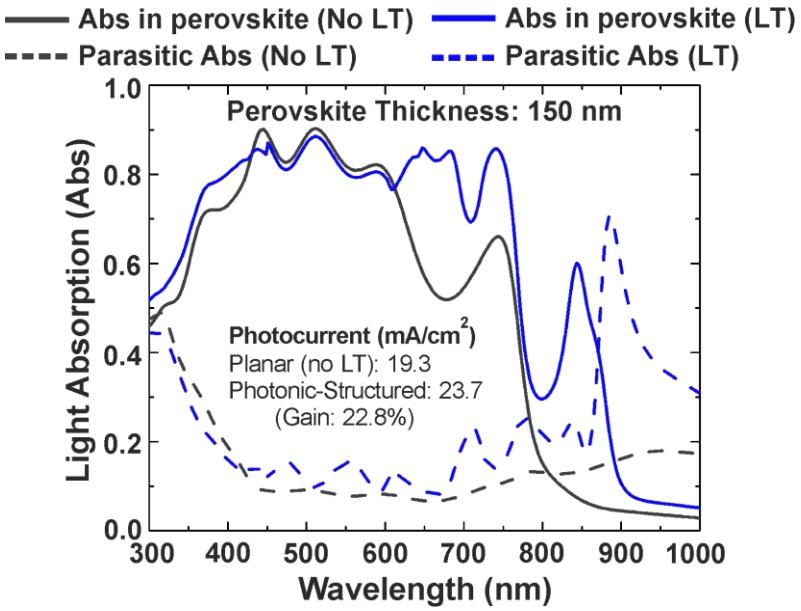

Figure S4: Light absorption spectra of the PSCs with (LT) or without (Planar reference) optimized photonic structures, for perovskite thickness of 150 nm in superstrate cell configuration, with a metal contact made of Au (see Figure 1,a). Here we show the absorption occurring only in the perovskite layer (solid lines) and that occurring in the other layers (parasitic) of the devices (dash lines).

As such, our LT structuring model is applicable and remains consistent for thicknesses smaller than the ones (300 and 500 nm) addressed in the manuscript. However, the absolute photocurrent for the LT-enhanced PSC with 150 nm perovskite thickness (23.7 mA/cm^2) is lower than that of the planar PSCs (no LT) with conventional thick 500 nm perovskite (25.1 mA/cm^2), whereas the LT-enhanced PSCs with 300 nm perovskite thickness (27.2 mA/cm^2) outperform the conventional thick planar PSCs (see Table S1).

S2. Electrical Modelling

The electrical simulations use as input the photo-generated charge carrier spatial distributions computed from the optical simulations described in the previous section. Considering such input, the present electrical models employ the classical drift-diffusion formalism, numerically computed via the Finite Element

Method (FEM) or the Finite Volume Method (FVM) implemented in different mesh-based charge transport solvers [18–20]. This is a physics-based electrical simulation tool for semiconductor devices that self-consistently solves the system of equations presented below, describing the drift-diffusion equation for the current density (Eq. S3), Poisson's equation for the electrostatic potential (Eq. S4), and the continuity equations for charge conservation (Eq. S5):

$$\boldsymbol{J}_{n,p} = q\,\mu_{n,p}\boldsymbol{E}n/p \pm\ qD_{n,p}\nabla n/p \qquad \text{(S3)}$$

$$-\nabla\cdot(\epsilon\nabla\mathbf{V}) = \mathrm{q}\rho \qquad \text{(S4)}$$

$$\frac{\partial n/p}{\partial t} = \pm\frac{1}{q}\nabla\cdot\boldsymbol{J}_{n,p} - R_{n,p} + G_{n,p} \qquad \text{(S5)}$$

here *R* and *G* are, respectively, the recombination and generation rates per unit volume (*n* and *p* subscripts indicate electron or hole, respectively), *q* the electron charge, *n/p* the electron/hole carrier density, ρ the total charge density, μ mobility, *D* diffusivity, V the electrostatic potential and $\boldsymbol{E}$ the electric field. Here, $R = R_n = R_p$ and $G = G_n = G_p$ since only local recombination/generation processes are considered which have to conserve locally the total number of carriers. Generation and recombination are major factors in the calculation of carrier behavior in the material, and these processes depend on temperature, doping, the E-field, current density and carrier concentration. The carriers move under two competing processes, drift due to the applied E-field and diffusion due to density gradients, appearing as the two terms in Eq. S3. Various domains are created and partitioned along the simulation region. Insulators, semiconductors and conductors' properties are specified in the simulation. Semiconductors use multi-coefficient models to describe the fundamental properties, mobility and recombination processes that are inherent and specific to the material. These models are employed in each vertex of the finite element discretization of the simulation domain, and the set of three partial differential equations (S4) and (S5) is discretized using FEM, reformulating the problem in weak form by projecting to a basis of piecewise linear functions, or using FVM by enforcing current continuity locally. The numerical solution of the resulting nonlinear set of algebraic equations provides the electrostatic potential and the carrier densities in each vertex. In this fashion, complex physics problems whose system of equations are unsolvable analytically are tackled, and the method is widely used in other areas of engineering and physics. All simulations are conducted at a temperature of 300 K.

As described in the main manuscript, three different software packages were used for the electrical simulations: TiberCAD [18], Lumerical-CHARGE [19] and Sentaurus Tcad [20], for the realistic prediction of the PV performance of PSCs. Each solver requires adapting the simulation environment differently, as explained next for each case.

S2.1 TiberCAD

The transport simulations presented in sub-section 3.2.1 employed the drift-diffusion model implemented in the simulation software TiberCAD [18], discretized with FEM and employing a Newton method with line search for the solution of the non-linear equations. The model follows the previously-described formalism, based on the generalized van Roosbroeck equations consisting of a system of partial differential equations, namely the Poisson equation and the continuity equation for each carrier is considered. However, here the Poisson equation determines the electrostatic potential *V* from the sum of charge densities resulting from all free charged carriers *(n, p)* as well as from ionized donors (N_d^-) and acceptors (N_a^+). The continuity equations describe the transport of carriers included in the system. The carrier fluxes are written in terms of the gradient of quasi-Fermi potentials. Mobilities are assumed to be constant, with values used as fitting parameters. For the recombination terms, we use standard models, in particular bi-molecular (radiative) recombination and trap-assisted (Shockley-Read-Hall, SRH) recombination. The latter can be parameterized via explicitly introducing trap states, or via fixed SRH life times. In our fitting procedure, we used SRH lifetimes to keep the number of parameters small, and because trap density and capture cross-section are highly correlated (only their product enters the lifetime).

For the fitting procedure, a simple 3D-optical/1D-electrical model implemented in TiberCAD was used to extract the relevant electrical parameters (effective mass, bandgap, recombination properties, etc.) of the materials and refine the simulation model using a potentially-flexible planar PSC deposited on PET substrate with high efficiency (measured PCE=18.5%, see Figure S5). The parameters used are summarized in Table S2.

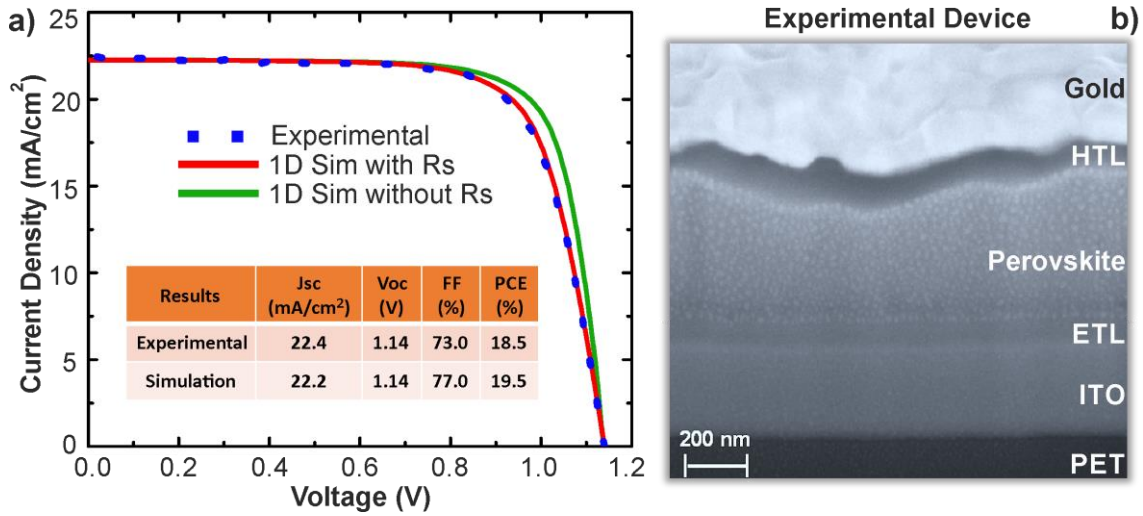

Figure S5: a) 1D device modelling and comparison with experimental planar flexible PSC with ~300 nm absorber thickness fabricated in the frame of the European project Apolo (https://project-apolo.eu/). The modelled JV curve in

red considers the effect of an additional series resistance, R_S, to better fit the device response. b) SEM image of the cross-section of the experimentally fabricated PSC on flexible PET substrate.

Table S2: *Parameters used for the electrical simulations in sub-section 3.2.1, considering the PSC structure of Figure 1 with a 300 nm thick Perovskite absorber.*

Material	Parameters	Value	Unit
Perovskite Absorber	Conduction band minimum	-3.93	eV
	Valence band maximum	-5.53	eV
	Bandgap	1.6	eV
	Effective density of states of the conduction band	1.5×10^{18}	cm^{-3}
	Effective density of states of the valence band	1.8×10^{18}	cm^{-3}
	Dielectric permittivity (relative)	25	
	Electron mobility	5	$cm^2 (Vs)^{-1}$
	Hole mobility	10	$cm^2 (Vs)^{-1}$
	Radiative recombination coefficient	2×10^{-9}	$cm^3 s^{-1}$
	SRH lifetime bulk	2.0×10^{-7}	s
Absorber/HTL Interface	Interface recombination parameter, *C*	10^{-19}	$cm^4 s^{-1}$

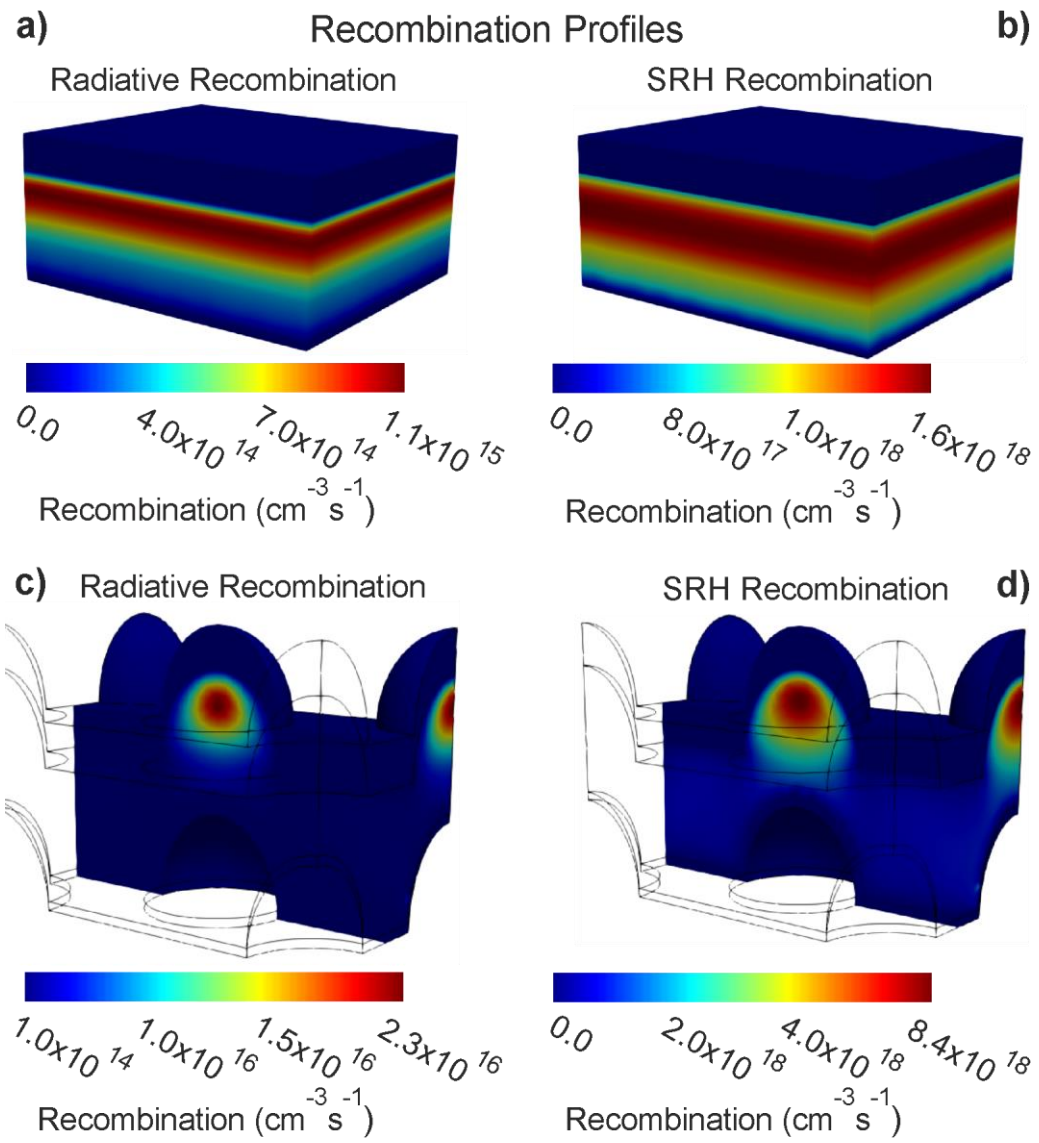

Figure. S6: Radiative (a,c) and SRH (b,d) recombination profiles, obtained from the 3D electrical simulations in TiberCAD, for the cases of optimized planar and structured PSCs, respectively, in substrate configuration with perovskite thickness of 300 nm and Au metal contact (see Table S1).

In an intermediate step, the optical generation files are read in Matlab and rewritten into an ASCII text file in column format "x y z G", which is read by TiberCAD. Based on the data points, a FEM mesh is generated, on which the data can be interpolated. Then, the transport simulation is performed on the device mesh, taking the generation data on the integration points by interpolation. The implementation is parallelized, which considerably accelerates the 3D simulations. In these simulations, a speedup factor of 11 and 19 has been measured, for 16 and 32 processes, respectively. A critical issue in such coupled simulations is the

translation of the generation rate from the optical to the electrical modeling, due to the grid change. For that, to minimize interpolation errors, we accurately matched the optical grid with the electrical grid.

The list of electronic properties that were used is presented in Table S2. Our simulation accounts for two main bulk recombination mechanisms: radiative and SRH, whose profiles along the planar and structured PSCs are shown in Figure S6 and commented in sub-section 3.2.1 of the manuscript. As expected, it can be seen that higher recombination occurs in the regions of higher carrier generation. In addition a bimolecular interface recombination rate at the perovskite/HTL interface is included, given by $R = C \cdot n_{PSK} p_{HTL}$, with parameter *C* given in units of $cm^4\ s^{-1}$, and n_{PSK} and p_{HTL} being the electron and hole densities in the two layers at the interface.

S2.2 Lumerical-CHARGE

As described in the main manuscript, 1D electrical simulations are sufficient to rigorously model conventional solar cells composed of a flat multi-layered structure, as the reference PSCs without LT features. In such common planar cases, the photo-generation profile varies only along the vertical direction (z axis), but is constant along the in-plane axes (x and y).

Nevertheless, when micro-structuring is applied to create the LT effects (see Figure 1, a), the photo-generation profile varies along the 3 spatial directions, as shown in section 3.1. In such cases, the use of 3D simulations would be the most realistic/exact procedure, to avoid spatially averaging the 3D photo-generation profiles in the x and/or y planes. However, 3D simulations require heavy time and memory costs when performed with the fine meshes used for the accurate FEM electrical modelling of photonic-structured PSCs. To circumvent this without significant loss of computational accuracy, 2D simulation routines were implemented which can be computed within a reasonable time and with the available processing/memory capabilities.

The electrical simulations performed in section 3.2.2 employed the Lumerical-CHARGE FEM solver [19]. This package receives the photo-generation distribution, *G(x,y,z)*, across the unit cell of the PSCs structure computed in the 3D optical simulations performed with the Lumerical-FDTD solver. The 3D photo-generation is then spatially averaged along the *y* axis to convert it to a 2D distribution, *G(x,z)*, which is imported to the 2D Lumerical-CHARGE program. The FEM calculations are then performed by first applying a 2D coarse mesh (with 30 nm maximum length constraints), and auto-mesh refinements (typically <10 times smaller than the geometrical sizes) across the regions with the highest E-field variations, as those where there are changes in doping density. A boundary condition controlling the bias is set on both Au metal (emitter contact) and TCO (base contact) where a steady-state DC sweep is run from 0.0 to 1.5 V applied voltage (0.025 V interval). Newton's numerical method was used for a self-consistent control of

the calculation, iterating between calculating the drift-diffusion equation and using it as an input to solve Poisson's (electrostatic potential) equation, and vice versa. This iteration was carried out until an absolute tolerance $<10^{-6}$ V is reached for convergence. The output containing the spatial information of the electrostatic potential, the electron-hole distribution, recombination rates, and mobility is used to compute the PSC characteristic JV curves. The list of electronic properties used in this simulation is represented in Table S3.

Table S3: *Electrical parameters considered for the materials (ITO/SnO_2/PSK/Spiro/Au) composing the planar and LT-enhanced PSCs with the geometrical parameters listed in Table S1 with Au and Ag metal contacts.*

	PSK	**SnO_2**	**Spiro$^+$**	**ITO**	**Au**	**Ag**
Intrinsic properties						
dc permittivity	6.5	9.0	3.0			
Φ (eV)	3.93	4.9	3.80	4.50	5.1	4.9
E_g (eV)	1.55	3.7	2.30			
$^{\#}m^*_e$	0.104	1.18	0.05			
$^{\#}m^*_h$	0.104	0.81	1.00			
$^{o}\mu_e$ (cm^2/V s)	30.0	0.2	2.0			
$^{o}\mu_h$ (cm^2/V s)	30.0	0.1	0.001			
$^{X}SRH_h$ (s)	5^{-9}	$5x10^{-9}$	$1x10^{-10}$			
$^{X}SRH_e$ (s)	5^{-9}	$1x10^{-9}$	$1x10^{-10}$			
Doping properties						
Dopant type	*n*	*p*	*p*			
Conc. (cm^{-3})	$7x10^{16}$	$1x10^{12}$	$2x10^{20}$			

In what concerns the recombination processes, the dominant recombination pathway in PSCs is found to be trap-assisted (SRH), as shown in Figure S6. Therefore, to simplify the simulations and minimize the number of involved parameters to the most fundamental ones, SRH was the only recombination process considered here, while the other two recombination processes (radiative and Auger) were taken to be negligible relative to SRH.

S2.3 Sentaurus Tcad

The electrical simulations presented in sub-section 3.2.3 employed the drift-diffusion model implemented in the commercial semiconductor software Sentaurus Tcad (from Synopsys Inc.) [20]. It is based on solving the drift-diffusion partial differential equations together with the Poisson equation (eqs. S3-5) in spatial dimensions with a finite volume method. Here we considered the list of electronic properties presented in Table S4.

The simulations performed using this tool focused on the interplay of interfaces and spatial distribution of the generation profiles, which is a crucial aspect for structured devices such as those analyzed here (see

Figure 1,a) patterned with the light-trapping features. To this end, we created 2D, planar 3D (Cuboid) and 3D-structures representing the superstrate configuration of Figure 1,a with Au contacts. A decisive question addressed here is whether a 3D-structure really requires a complete 3-D electrical simulation (with its corresponding CPU and Memory demand) or whether 1- or 2-D electrical simulations based on homogenized optical data could lead to very similar results, thus reducing the computational effort significantly.

To work on the 3D structure, the simulation flow had to be adapted to be able to synthesize the discrete topography from the provided geometric descriptions (see Table S1) and to integrate the provided 3D-generation data [$G(x,y,z)$, see section 3.1]. Especially the integration of the optical generation data proved challenging to align correctly. As the generation data was provided in a cubic voxel grid, but the geometric structure is continuous, simple overlaying would lead to aliasing effects at the interfaces, reducing the generated current. To counteract this problem, the generation data was pre-processed to constantly extrapolate the generation values at the interfaces outwards, to later intersect the data with the continuous geometric structure (see Figure S7).

The aliasing effects also play a role in the vertex-centered simulation mesh. Specifically, the discontinuous generation profile leads to problems of current over-accounting at the interfaces. The 1D simulations can be executed with a mesh resolution of 1000 steps per nanometer which does not lead to measurable over-accounting. However, this resolution cannot be maintained for the present 3D-simulations, in which the mesh resolution drops to 1 step per every 2 nanometers at the interfaces and 1 step every 20 nanometers in the bulk. Further explanations regarding data translation from Lumerical-FDTD to Sentaurus Tcad solver are given in the following sub-section.

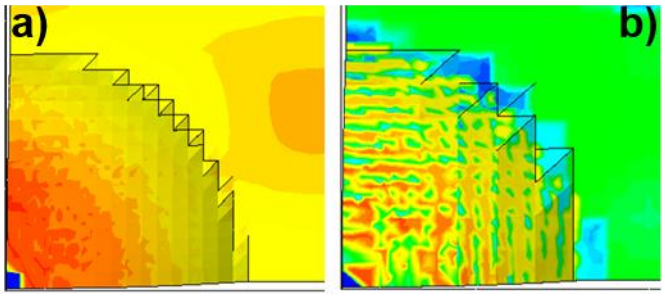

Figure. S7. Impact of extrapolation on the interface generation rate (G). *a)* - with extrapolated generation. *b)* - without extrapolated data.

The resolution of the discretized mesh was increased until the numerical integration of the generation rate J_{PH} converged. This provided a sufficiently accurate spatially resolved representation of the generation data provided by the optical simulations (see Figure 2, b) while keeping the required computational effort to run the simulations manageable. To focus on the effect of the interfaces between the absorber and HTL / ETL,

the physical parameters were chosen such as to minimize effects due to other factors impacting the device performance, e.g. band energy mismatch or low mobility in the ETL. Outside the perovskite layer, the device can be considered idealized, except for a serial resistance of 3.3 $m\Omega cm^{-2}$.

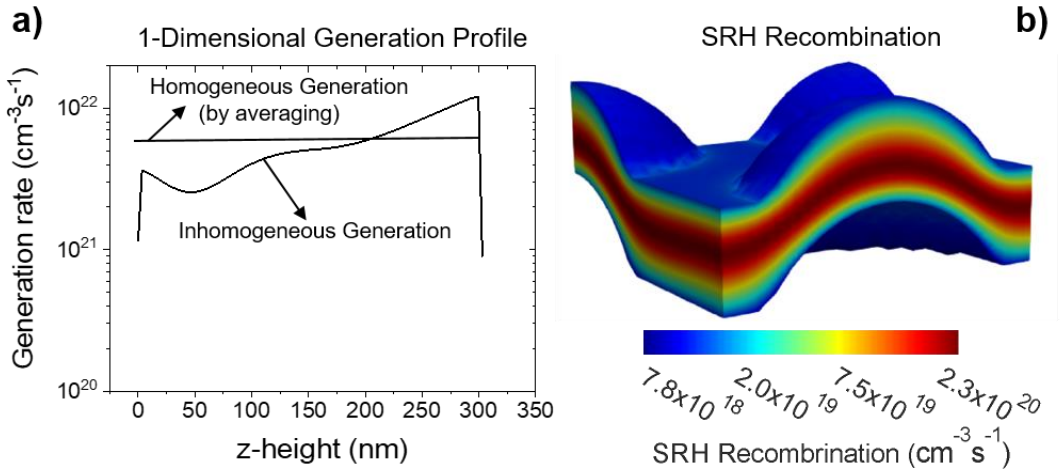

Figure. S8: The normalized 1D generation profiles (a) across the absorber thickness, as well as the SRH recombination profile (b) at the maximum power point obtained in Sentaurus Tcad electrical modelling.

Figure S8,a shows an example of the normalized 1D generation profiles of the inhomogeneous and homogeneous (averaged constant field) generation functions that were created from the 3D-optically computed *G(x,y,z)* data, by first planarizing the 3D generation profile, *G*, and then integrating along the in-plane directions *(x,y)*. Such profiles were used for the 1D electrical simulations in Sentaurus Tcad in sub-section 3.2.3 of the manuscript. Figure S8,b depicts the cross-section of the SRH recombination profile across the perovskite absorber, and in the HTL/ETL interface surfaces, resulting from the 3D electrical simulations in Sentaurus Tcad in sub-section 3.2.3.

***Table S4**: Parameters used for the electrical simulations in sub-section 3.2.3, considering the PSC structure of Figure 1,a with a 300 nm thick perovskite absorber.*

Material	Parameters	Value	Unit
Perovskite Absorber	Conduction band minimum	-4.0	eV
	Valence band maximum	-5.6	eV
	Bandgap	1.6	eV
	Effective density of states of conduction band	$5x10^{18}$	cm^{-3}
	Effective density of states of valence band	$5x10^{18}$	cm^{-3}
	Dielectric permittivity (relative)	25	
	Electron mobility	10	$cm^2 (Vs)^{-1}$
	Hole mobility	10	$cm^2 (Vs)^{-1}$

	Radiative recombination coefficient	10^{-11}	$cm^3\ s^{-1}$
	SRH lifetime bulk	$2.5x10^{-7}$	s
Absorber/HTL or ETL Interface	SRH surface recombination velocity, S_0	140	$cm\ s^{-1}$

S2.3.1 Data translation from optical to electrical solvers

Figure S9 shows the process of extracting the optically determined generation rate *G* from Lumerical-FDTD and integrating it into the FEM mesh for various drift diffusion solvers. Given that the Lumerical data is extracted on a cubic lattice (voxel based), this can lead to sampling problems when it is transferred into a Tetrahedron based *unstructured* FEM-Mesh (note on the differences of $J_{PH,\ Lumiercal}$ and $J_{PH,\ FEM} = J_{SC,Sentaurus}$).

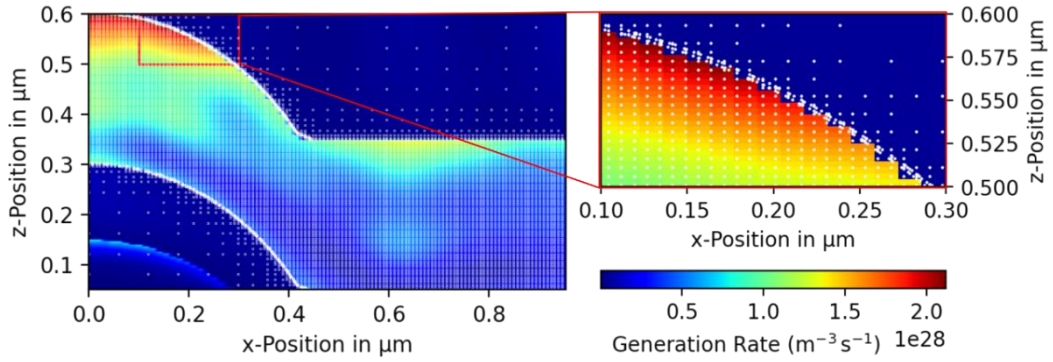

Figure. S9: 2D-Slice through the volumetric generation rate. The white dots correspond to sampling points of a high-resolution FEM-Mesh.

In the enlarged portion it can be seen that the sampling of a voxel-based generation rate with an unstructured grid can lead to sampling errors along inclined surfaces. Given that the generation rate has a strong gradient along these surfaces, this problem needs to be mitigated to achieve a good agreement between the J_{PH} of the source data and the target mesh. Possible solutions can include further interpolation or, as has been described in Figure S7, extrapolation of the generation rate at the interface into the z-Direction. For the simulation in Sentaurus the extrapolation strategy has improved the convergence with J_{PH} of the source data. This strategy also maintains the strong generation rate gradient at the interface, which might be diluted with interpolation.

The second challenge is the limited FEM mesh resolution, which leads to under-sampling of the Lumerical data. Neither the Mesh in Figure S7 or Figure S9 show a point density similar to the source voxel density. That means that not only are all voxels not sampled equally, but some of the data does not get sampled at all. If the gradient between the sampled points is constant, this can be mitigated by the intrinsic extrapolation of the FEM mesh. If, however, the generation rate shows strong discontinuities within such an area, this

can lead to discrepancies between the J_{PH} of the source data and the FEM mesh. Especially at the interface towards the direction of illumination, large gradients in the generation rate are present, while at the same time the larger local generation level is comparatively high, leading to potentially large deviations in J_{PH}. Such areas are especially sensitive to under-sampling. This has been addressed by finding a sufficiently similar J_{PH} between FEM-Mesh and the source data.

S3. References

(1) Phillips, L. J.; Rashed, A. M.; Treharne, R. E.; Kay, J.; Yates, P.; Mitrovic, I. Z.; Weerakkody, A.; Hall, S.; Durose, K. Dispersion Relation Data for Methylammonium Lead Triiodide Perovskite Deposited on a (100) Silicon Wafer Using a Two-Step Vapour-Phase Reaction Process. *Data Br.* **2015**, *5*, 926–928. https://doi.org/10.1016/J.DIB.2015.10.026.

(2) Phillips, L. J.; Rashed, A. M.; Treharne, R. E.; Kay, J.; Yates, P.; Mitrovic, I. Z.; Weerakkody, A.; Hall, S.; Durose, K. Maximizing the Optical Performance of Planar CH3NH3PbI3 Hybrid Perovskite Heterojunction Stacks. *Sol. Energy Mater. Sol. Cells* **2016**, *147*, 327–333. https://doi.org/10.1016/J.SOLMAT.2015.10.007.

(3) Haque, S.; Mendes, M. J.; Sanchez-Sobrado, O.; Águas, H.; Fortunato, E.; Martins, R. Photonic-Structured TiO2 for High-Efficiency, Flexible and Stable Perovskite Solar Cells. *Nano Energy* **2019**, *59*, 91–101. https://doi.org/10.1016/J.NANOEN.2019.02.023.

(4) Haque, S.; Alexandre, M.; Mendes, M. J.; Águas, H.; Fortunato, E.; Martins, R. Design of Wave-Optical Structured Substrates for Ultra-Thin Perovskite Solar Cells. *Appl. Mater. Today* **2020**, *20*, 100720. https://doi.org/10.1016/J.APMT.2020.100720.

(5) *Nanophotonic FDTD Simulation Software - Lumerical FDTD*. https://www.lumerical.com/products/fdtd/ (accessed 2022-06-12).

(6) Mendes, M. J.; Araújo, A.; Vicente, A.; Águas, H.; Ferreira, I.; Fortunato, E.; Martins, R. Design of Optimized Wave-Optical Spheroidal Nanostructures for Photonic-Enhanced Solar Cells. *Nano Energy* **2016**, *26*, 286–296. https://doi.org/10.1016/J.NANOEN.2016.05.038.

(7) Mendes, M. J.; Haque, S.; Sanchez-Sobrado, O.; Araújo, A.; Águas, H.; Fortunato, E.; Martins, R. Optimal-Enhanced Solar Cell Ultra-Thinning with Broadband Nanophotonic Light Capture. *iScience* **2018**, *3*, 238–254. https://doi.org/10.1016/j.isci.2018.04.018.

(8) Kaiser, C.; Zeiske, S.; Meredith, P.; Armin, A. Determining Ultralow Absorption Coefficients of Organic Semiconductors from the Sub-Bandgap Photovoltaic External Quantum Efficiency. *Adv. Opt. Mater.* **2020**, *8* (1), 1901542. https://doi.org/10.1002/adom.201901542.

(9) Caselli, V. M.; Wei, Z.; Ackermans, M. M.; Hutter, E. M.; Ehrler, B.; Savenije, T. J. Charge Carrier Dynamics upon Sub-Bandgap Excitation in Methylammonium Lead Iodide Thin Films: Effects of Urbach Tail, Deep Defects, and Two-Photon Absorption. *ACS Energy Lett.* **2020**, *5* (12), 3821–3827. https://doi.org/10.1021/ACSENERGYLETT.0C02067.

(10) Teixeira, J. P.; Salomé, P. M. P.; Alves, B.; Edoff, M.; Leitão, J. P. Evidence of Limiting Effects of Fluctuating Potentials on VOC of Cu(In,Ga)Se2 Thin-Film Solar Cells. *Phys. Rev. Appl.* **2019**, *11* (5), 054013. https://doi.org/10.1103/PhysRevApplied.11.054013.

(11) Yin, G.; Manley, P.; Schmid, M. Light Trapping in Ultrathin CuIn 1-x Ga x Se 2 Solar Cells by Dielectric Nanoparticles. *Sol. Energy* **2018**, *163* (January), 443–452. https://doi.org/10.1016/j.solener.2018.01.096.

(12) Morawiec, S.; Mendes, M. J.; Filonovich, S. A.; Mateus, T.; Mirabella, S.; Águas, H.; Ferreira, I.; Simone, F.; Fortunato, E.; Martins, R.; Priolo, F.; Crupi, I. Broadband Photocurrent Enhancement in A-Si:H Solar Cells with Plasmonic Back Reflectors. *Opt. Express* **2014**, *22* (S4), A1059. https://doi.org/10.1364/OE.22.0A1059.

(13) Mendes, M. J.; Morawiec, S.; Mateus, T.; Lyubchyk, A.; Águas, H.; Ferreira, I.; Fortunato, E.; Martins, R.; Priolo, F.; Crupi, I. Broadband Light Trapping in Thin Film Solar Cells with Self-Organized Plasmonic Nano-Colloids. *Nanotechnology* **2015**, *26* (13), 135202. https://doi.org/10.1088/0957-4484/26/13/135202.

(14) Ginting, R. T.; Kaur, S.; Lim, D.-K.; Kim, J.-M.; Lee, J. H.; Lee, S. H.; Kang, J.-W. Plasmonic Effect of Gold Nanostars in Highly Efficient Organic and Perovskite Solar Cells. *ACS Appl. Mater. Interfaces* **2017**, *9* (41), 36111–36118. https://doi.org/10.1021/acsami.7b11084.

(15) Mendes, M. J.; Morawiec, S.; Simone, F.; Priolo, F.; Crupi, I. Colloidal Plasmonic Back Reflectors for Light Trapping in Solar Cells. *Nanoscale* **2014**, *6* (9), 4796–4805. https://doi.org/10.1039/c3nr06768h.

(16) R. Erwin, W.; F. Zarick, H.; M. Talbert, E.; Rizia Bardhan. Light Trapping in Mesoporous Solar Cells with Plasmonic Nanostructures. *Energy Environ. Sci.* **2016**, *9* (5), 1577–1601. https://doi.org/10.1039/C5EE03847B.

(17) Maier, S. A. *Plasmonics: Fundamentals and Applications*; Springer, 2007. https://doi.org/10.1007/0-387-37825-1.

(18) *tiberCAD | DEVELOPER COMMUNITY*. http://www.tibercad.org/ (accessed 2022-06-12).

(19) *CHARGE solver introduction – Lumerical Support*. https://support.lumerical.com/hc/en-us/articles/360034917693-CHARGE-solver-introduction (accessed 2022-06-12).

(20) *Sentaurus Device - Technology Computer Aided Design (TCAD) | Synopsys*. https://www.synopsys.com/silicon/tcad/device-simulation/sentaurus-device.html (accessed 2022-06-12).